2015

Adhesion mechanisms of Ti-6Al-4V to PVD coatings

Liang Jin
University of Windsor

Adhesion mechanisms of Ti-6Al-4V to PVD coatings

By

Liang Jin

A Thesis
Submitted to the Faculty of Graduate Studies
through Mechanical, Automotive & Materials Engineering
in Partial Fulfillment of the Requirements for
the Degree of Master of Applied Science
at the University of Windsor

Windsor, Ontario, Canada

2015

Adhesion mechanisms of Ti-6Al-4V to PVD coatings

BY

Liang Jin

APPROVED BY:

H. Hu

Department of Mechanical, Automotive, and Materials Engineering

W. Abdul-Kader

Department of Mechanical, Automotive, and Materials Engineering

A. R. Riahi, Advisor

Department of Mechanical, Automotive, and Materials Engineering

A. Edrisy, Advisor

Department of Mechanical, Automotive, and Materials Engineering

January 23, 2015

DECLARATION OF CO-AUTORSHIP/PREVIOUS PUBLICATION

I. Co-Authorship Declaration

I hereby certify that this research incorporates material that is the result of a joint research undertaken in collaboration with K. Farokhzadeh from Department of Mechanical, Automotive, and Materials Engineering at University of Windsor under the supervision of Dr. A.R. Riahi and Dr. A. Edrisy. The research collaboration is covered in Chapter 3, 4, and 5 of the thesis.

I am aware of the University of Windsor Senate Policy on Authorship and I certify that I have properly acknowledged the contributions of other researchers to my thesis, and have obtained permission from each of the co-authors to include the above materials in my thesis.

I certify that, with the above qualification, this thesis, and the research to which it refers, is the product of my own work.

II. Declaration of Previous Publication

This thesis includes 2 original papers that have been previously published/ submitted for publication in peer reviewed journals, as follows:

Thesis Chapter	Publication title/full citation	Publication status
Chapter 2, 3, 4, 5, 6	L. Jin, A.R. Riahi, K. Farokhzadeh, A. Edrisy, Investigation on interfacial adhesion of Ti–6Al–4V/nitride coatings, Surface and Coatings Technology, Volume 260, December 2014, Pages 155–167.	Published
Chapter 2, 3, 4,	L. Jin, A.R. Riahi, A. Edrisy, Analysis of Ti-6Al-4V	Manuscript

5,6	adhesion to AISI 52100 steel and TiN during unlubricated sliding contact, Tribology International, 2015.	submitted for minor revision

I certify that I have obtained a written permission from the copyright owner(s) to include the above published material(s) in my thesis. I certify that the above material describes work completed during my registration as graduate student at the University of Windsor.

I declare that, to the best of my knowledge, my thesis does not infringe upon anyone's copyright nor violate any proprietary rights and that any ideas, techniques, quotations, or any other material from the work of other people included in my thesis, published or otherwise, are fully acknowledged in accordance with the standard referencing practices. Furthermore, to the extent that I have included copyrighted material that surpasses the bounds of fair dealing within the meaning of the Canada Copyright Act, I certify that I have obtained a written permission from the copyright owner(s) to include such material(s) in my thesis.

ABSTRACT

The adhesion mechanisms of titanium alloy Ti-6Al-4V to AISI 52100 steel and AlTiN, TiN and CrN nitride coating were studied. It was found that the transferred Ti-6Al-4V had a layered amorphous structure in which nanocrystalline and polycrystalline oxides were embedded. High resolution TEM (HRTEM), electron diffraction, and fast Fourier transform (FFT) investigations revealed the presence of nanocrystalline TiO (C2/m) at the steel/transfer layer and AlTiN/transfer layer interface. However only α-titanium (P63/mmc) was detected at the TiN/transfer layer interface and CrN/transfer layer. This observation explains that the coefficient of friction between TiN and Ti-6Al-4V as well as CrN and Ti-6Al-4V reached the threshold value within shorter distance. The different adhesion behavior of Ti-6Al-4V to different counterface materials can be related to low misfit between α-titanium and TiN and CrN crystals.

DEDICATION

I dedicate this thesis to my loving parents and my wife for their support and unconditional love.

I dedicate this thesis work to my advisors Dr. A. R. Riahi and Dr. A. Edrisy for their support and guidance in my research career.

ACKNOWLEDGEMENTS

I would like to give special thanks to my advisors Dr. A. R. Riahi and Dr. A. Edrisy. They provide me the chance to come to Canada two years. They provide excellent guidance and support to my research. They let me have the research experience titanium and tribology field.

I also would to thank my committee members, Dr. Hu and Dr. Abdul-Kader for their comments in improving my research and thesis. Many thanks to K. Farokhzadeh and other colleagues in the group of Dr. Riahi and Dr. Edrisy for help in my research.

TABLE OF CONTENTS

LIST OF TABLES

LIST OF FIGURES

LIST OF ABBREVIATIONS, SYMBOLS

ASTM	American Society for Testing and Materials
BSE	backscattered electron
CBED	convergent beam electron diffraction
COF	coefficient of friction
EDS	energy dispersive spectroscopy
EELS	electron energy loss spectroscopy
FIB	focused ion beam
HRTEM	high resolution transmission electron microscopy
SE	secondary electron
SEM	scanning electron microscopy
STEM	scanning transmission electron microscopy
TEM	transmission electron microscopy
PVD	physical vapor deposition
CVD	chemical vapor deposition
FCC	face center cubic
HCP	hexagonal close packing

CHAPTER 1 INTRODUCTION

1.1 Overview

The focus of this research is the adhesion mechanisms of Ti-6Al-4V to different nitride coatings. The background information on this study is briefly presented in this chapter. The motivations and objectives of this research are also stated.

1.2 Motivation

Titanium alloys are applied widely in the aerospace, transportation, biomedical, chemical, and petroleum industries, because it possesses remarkable properties, including high specific strength and excellent corrosion resistance, biocompatibility and fatigue strength. Different types of titanium alloys can be derived for the phase transformations of titanium alloys occur at around 880°C. Alloying elements are added to manipulate both physical and mechanical properties of titanium alloy by altering the phase composition. Alloying elements are divided into three major categories: α stabilizer, β isomorphous stabilizer and β eutectoid stabilizer. The α stabilizers including Al, O and N, are more soluble in the α phase and raise the β transus temperature. Eutectoid β stabilizers such as Fe, Cr and Cu are added to retain a fully β structure after quenching. 4-6% isomorphous β stabilizers such as Mo, V and W are added to allow the existence of β phase at room temperature after quenching. Single-phase α alloys are applied mainly in where corrosion resistance is the first concern. α + β alloys provide a balance combination of mechanical properties such as strength, toughness, high temperature

properties, as well as excellent corrosion resistance properties. Near-β alloys meet the requirements of excellent strength with the sufficient toughness and fatigue resistance, thus find their application in aerospace applications.

Ti-6Al-4V possesses good physical and mechanical properties, as well as good formability. Thus, Ti-6Al-4V becomes the most widely applied titanium alloy since it is developed. It contains β stabilizers (4 wt% V) and a solid solution strengthener (6 wt% Al) in the Ti alloy. However its further application is limited by poor wear resistance property.

Physical vapor deposition processes (PVD) are widely applied to deposit thin films and coatings with the thickness range of a few nanometers to a few micrometers. PVD processes are also applied to deposit compounds by employing reactive deposition. The compounds are often formed by the reaction of the target materials and the ambient gas such as oxygen or nitrogen. Arc vapor deposition is a PVD process, which is commonly used to deposit hard coatings by using a high current, low voltage arc to vaporize the target material. The vaporized material is highly ionized and usually the substrate is biased to attract the ionized material. Nitride coatings produced by cathodic arc vapor deposition are widely applied in cutting and bearing tools. However, their applications in machining titanium are limited because of the adhesion tendency of titanium alloys, which reduce the tool life significantly. The mechanisms of adhesion of titanium alloys to nitride coatings are not fully understood.

1.3 Research objective

The aim of this research is to analysis the α + β Ti-6Al-4V titanium alloy adhesion to different nitride coatings. In this work, AlTiN, TiN and CrN coatings, commonly utilized for machining and bearing applications, as well as AISI 52100 steel are selected as counterface materials for Ti-6Al-4V. Their performance in terms of adhesion behavior and coefficient of friction during both ball-on-disk and adhesion tests were evaluated and compared. The objective of this research was to understand the mechanisms of adhesion and transfer of Ti-6Al-4V to different counterface materials during the initial stages of sliding.

CHAPTER 2 REVIEW OF LITERATURE

2.1 Overview

Microstructures, mechanical properties of commonly applied titanium and its alloys, in particular Ti-6Al-4V are summarized in this chapter. The tribological properties of nitride coatings are reviewed. The applications of PVD coatings in machining titanium alloys are also reviewed briefly. The adhesion mechanisms of Ti-6Al-4V during sliding contact during break-in period are reviewed in details.

2.2 Titanium and titanium alloys

Titanium, ranking the fourth abundant structural metal (0.6%) in the earth, only after aluminum, iron, and magnesium, has drawn research interests in its alloying, properties, and applications since in late 1940's [1]. The mineral sources mainly include ilmentite (FeTiO3) and rutile (TiO2). Researches have revealed that titanium alloys possess remarkable properties including high specific strength and corrosion resistance, biocompatibility and fatigue strength, thus, have now found a wide range of applications in variety industries [1, 2]. Among the different applications of titanium and titanium alloys, airframes and aero-engines are the two areas, which first introduce titanium and titanium alloys into industrial field due to their excellent structural efficiency and mechanical properties at elevated temperature [2, 3]. Chemical and petroleum industries have seen titanium and its alloys as common choices because of their excellent corrosion resistant properties [4]. There is also an increasing application of titanium and its alloys

as building materials, because of their high specific strength, low density, and low modulus [5]. Biomedical industry is another area where the application of titanium alloys is well established. The main advantage of titanium alloys as implant materials is biocompatibility, superior fatigue strength and low elastic modulus [1, 2]. Other areas where titanium has been widely used includes racing cars and trucks, golf club heads, tennis rackets and racing bicycles, etc [2].

2.2.1 Crystal structure and alloy elements

Pure titanium has a hexagonal close packed (HCP) structure, which is called α-titanium [1, 2]. The c/a ratio of HCP α-titanium is 1.587 at room temperature, which is lower than an ideally HCP lattice with the c/a ratio is 1.633 [1, 2]. The smaller distance between two basal planes, which leads to the atom packing density in prism planes became higher and close to that in basal planes. This causes an increased number of slip systems in α-titanium and results in superior ductility compare to other HCP metals [2]. However, hexagonal close packed (HCP) structure will transfer to body-centered cubic structure, which is called β-titanium. The transit temperature for pure titanium is approximately 882 °C [1]. The existence of this phase transformation provides the possibility of obtaining different titanium alloys with a variety of properties by adding different alloying elements and various heat treatments. The alloying elements of titanium can be classified as neutral, α-stabilizers and β-stabilizers. The α-stabilizers elements can elevate α/β the phase transformation temperature. The β-stabilizers can

lower this phase transformation temperature [2]. Al is the most common applied α-stabilizer. β-stabilizers can be divided into β-isomorphous and β-eutectic elements two subcategories. Mo, V and Nb are the most common β-isomorphous elements, which can stabilize β phase at room temperature [1, 2]. β-eutectic, including Fe, Mn, Cr, Co, Ni, Cu and Si, can stabilize β phase by forming intermetallic compounds. Neutral alloying elements (do not effect phase transformation), such as Zr and Sn, are added mainly to strengthen α-titanium [1].

2.2.2 Mechanical, wear and friction properties of Ti-6Al-4V

Titanium alloys applied in this research is Ti-6Al-4V. The mechanical, physical and thermal properties are listed in Table 2.1 [4]. Ti-6Al-4V possesses an exceptional strength, ductility, fatigue, and fracture properties. The ELI version of this popular alloy has especially high fracture toughness values and excellent damage tolerance properties and it also has a good balance of productivity. However, their poor wear resistance and susceptibility to galling results in components' failure when sliding contact is unavoidable and thus prevents extensive application of titanium alloys [5, 6].

Bloyce et al attributed the poor tribological behavior of titanium to three factors [3]. The first is the low D-valence bonding electron configuration, which leads to titanium more reactive and confers a high friction coefficient. The second is the modified HCP crystal structure, which allows several slip systems to operate with a close critical shear stress. The last is the relative low tensile and shear strength of titanium alloys compare to

common applied steel counterface. Another two factors that contribute to the high wear rate of titanium alloys, according to Molinari et al. [7, 8], are low work hardening, which results in adhesion, abrasion, and delamination, and the easily-removed oxides formed during sliding, which cannot protect the alloy effectively. They found that the main wear mechanisms for titanium alloys were oxidation-dominated and delamination-dominated wear and a minimum wear rate was achieved at medium sliding speeds corresponding to a transition from oxidation to delamination wear [9]. Thus, the fracture occurs in the titanium rather than at the junction, resulting in a relatively large amount of metal transfer and hence higher wear rates [10].

The effect of the counterface material on the adhesion and wear behavior of titanium alloys has been studied by several researchers. Strafellini et al. [8] reported that the wear rate of Ti-6Al-4V was higher when sliding against AISI M2 steel, compared to self-mating sliding conditions due to the abrasive action of hard carbide particles in the steel microstructure. They highlighted that severe oxidation and transfer of Ti-6Al-4V occurred during dry sliding wear of the alloy irrespective of the counterface material and found that the transfer layers and the generated wear debris particles mainly consisted of TiO and α-Ti according to X-ray diffraction (XRD) analyses. A tribochemical wear mechanism was proposed by Dong et al. [10] for Ti-6Al-4V surfaces sliding against alumina. They found that the tribolayers on the surface of alumina counterpart consisted of intermetallics such as Ti_3Al, a reduction product of alumina by titanium. They also

reported a strong bonding between the tribolayer and the counterface possibly due to the mutual diffusion and formation of the titanium aluminides at the interface.

Qu et al. [11] studied the tribological behavior of Ti-6Al-4V against ceramic (silicon nitride, alumina), polymer (polytetrafluoroethylene) and metal (stainless steel) counterparts. They reported that titanium transferred to steel, polymer, and alumina counterface surfaces; however, when sliding against silicon nitride coatings, Al in the Ti-6Al-4V alloy formed chemical compounds and Ti transferred to the counterface in the form of amorphous titanium oxides.

The findings of Jaffery et al. and Jawaid et al [12, 13] revealed that the adhesion tendency of titanium alloys is also responsible for chipping and flaking of the coated cutting tools during machining operations due to the periodic formation and spallation of the titanium transfer layer. They suggested that the low thermal conductivity of titanium alloys was another influential factor for the significant material transfer to the counterparts.

Although the strong adhesion tendency of titanium has been confirmed by its extensive transfer to various mating materials such as steels, aluminum alloys, ceramic coatings, and polymers under sliding conditions [14, 15], the micromechanisms involved in the transfer of titanium to counterface surfaces remain unclear.

2.3 Metal-metal and metal-ceramic adhesion mechanisms

It is well known that the friction will result in the energy dissipation and the

damage of surface, thus, friction has been studied for more than one hundred years to minimize energy loss and protect the contacted surfaces [16].

In engineering design field, wear is another fundamental discipline regarding safety and energy saving issues. The areas, which have special interest in wear and friction, include bearings, brakes, tires, clutches and engines. Increasing researches have been seen in biomedical, micro and nanotechnology.

Adhesion has a strong influence on the wear and friction behavior of engineering materials. Ferrante and Smith [17] first pointed out that the adhesion of aluminum to magnesium took place when the distance between two surfaces is lower than 0.2 nm, which is proved to be a critical separation distance to avoid adhesive wear between metals. Bowden and Tabor [18] first noticed that the real contact area is at least one order magnitude smaller the nominal contact area due to the surface roughness. Thus, the contact mechanics became one of the foundations of a modern tribology research. Hertz provided solutions to the calculation of contact pressure between two elastic curved surfaces. Derjagin, Müller, and Toporov [19] proposed another theory to explain adhesive contact. Later Bowden and Tabor [18] summarized the law of abrasive wear that the amount of wear proportional to load and sliding distance, however, is inversely proportional to the hardness of the weaker materials. Archard [20] developed equations to estimate the temperature at contacted asperities. Tabor and Rabinowicz [21] examined and expanded that abrasive to the adhesive wear. Recent researches explained the

frictional and abrasive phenomenon at atomic level. Numerical simulation methods further found the application of the friction and wear study to micro-technology [22]. Friction, wear and lubrication are the three main research fields in tribological research.

A well-disguised tendency for all materials to mutually adhere when brought into a close contact is the basic cause of adhesive wear. Adhesive wear is the fundamental cause of failure of most metal sliding contacts and therefore its effective prevention is essential to proper functioning of engineering [19].

The adhesion between contacted asperities can result in a large component of frictional force and the deformation and remove of the asperities, which often forms the transfer materials and wear particles in the following sliding process [19]. This strong adhesion, material transfer and particle forming mechanism often occur and predominant the wear process between identical metals. The adhesion force increases dramatically after the surface contamination removed in the early stage of sliding contact, which will result in the friction force increased abruptly [23].

The strength of the junction is usually higher than that of the contacted metals. Thus, after the sliding starts, the severe shear deformation took place in the metal side. The plastic deformation of contacted asperities will result in the work hardening of the contacted metals. The deformation of bond asperities contribute more than the fracture of asperities [19].

2.3.1 Metal-metal adhesion mechanisms

Adhesive wear usually results in high wear rates and a large fluctuation in the coefficient of friction [24]. Adhesive wear can damage the contacted surfaces rapidly by the transfer of materials and in extreme case result in seizure. Metals are well known for they subjected to adhesive wear. The breakdown of lubricant often occurs between the sliding metals and result in the contact of sliding surface [25].

Research revealed that the adhesion tendency between metals can be influenced by the mutual solubility and the relative atomic size [25]. Although the strongest adhesion observed between the same and similar materials, for example titanium to titanium, different and unlike metals can also result in strong adhesion. The metal transfer from the weaker material to the stronger one can happen between different combinations of metals at low or moderate temperatures [24].

The strong adhesion between metals can be triggered by the electron transfer between contact surfaces [26]. The abundant free electrons in metals can exchange between to contacted surfaces within several nanometers range. It is proved that when the two surfaces in contact are close enough, i.e. the distance between the two surfaces is smaller than 1 nm, the free electrons can move from the one with higher electron density to the another one [25]. This transfer of electron can bond the two solids together, however, it is also proved that the adhesion force calculation according to this theory is considerably higher than the experimental values as a result of the difficulty of

determining the real contacted area between atoms [27].

All major engineer metals display a strong tendency to transfer to the counterface materials; however, this can be predicted by the different combination of metals. It is showed that the crystal structure of metals have effect on the adhesion behavior during sliding contact [26]. The adhesion behavior is also controlled by the mechanical properties of contacted surfaces. It is reported that metals with high hardness, elastic modulus and surface energy usually show low adhesion tendency [27].

When two solid surfaces come into contact, plastic deformation may occur at contacted asperities due to plastic deformation. Another factor that can control the adhesion between of metals is the chemical reactivity of the contacted metals. For example, noble metals such as gold and platinum show weaker adhesion tendency in vacuum than chemical active metals, e.g. aluminum [25].

2.3.2 Metal-ceramic adhesion mechanisms

The research attention has been drawn on the topic of adhesion between metals and ceramic, because of the increasing application of ceramic coatings in machining, bearings and superconductors. Klomp and Vrugt [28] further employed the measurement of electromotive force between ceramics and metals and found that the d-valence electrons in metals involved the most in the physical reaction between metals and ceramics. Buckley [29] suggested that the adhesion strength between ceramics and metals increased as the increase of the percentage of d-valence electrons in metals. According to Miyoshi

[30], the predominant factor of metal-ceramic adhesion is the hardness of metal.

Adhesion between metals and ceramics can be strong under dry sliding condition, especially with certain combinations. The chemical affinity is the main control factor in the adhesion behavior between metals and ceramics [31]. It is reported that nitride and oxide coatings can reduce the coefficients of friction when sliding against metals [30]. When metals bond to ceramics, the rupture of the bonded asperities usually takes place within the metal side due to the lower cohesive strength of metals [30].

The wide application of ceramic in cutting tools and bearing materials provide the chance to reduce the wear and friction by choosing the different combination of contacted materials. The ceramic coatings can reduce the wear and friction by avoiding the similar or identical materials in contact with each other. The study of mutual solubility revealed that chemical active metals have stronger tendency to adhere to the ceramics compared to the passive or inert ones, thus resulting in a higher coefficient of friction and wear rate [31].

To conclude, after the contact load is sufficient to result in the plastic deformation of the bond asperities [27]. The electron transfer will result in the bond of contacted asperities. The adhesion behavior of metals is controlled by the crystal structures, mechanical properties and chemical reactivity. The oxides films forming on the metal surface have a critical thickness, over which the oxide films can reduce the coefficient of friction by replacing the strong adhesion between metals to van der Waals forces [25].

2.3.3 Foundations of break-in periods in wear and friction

The term break-in will be used primarily in connection with changes in friction and wear, which occur in tribosystems before steady state is reached. If no form of steady state is observed, then no break-in period can be defined for the given system. If, however, tribologically similar systems are known to reach a steady state reproducibly, then the phrase “incompletely break-in” or “partially broken-in” can be used. Break-in can be used to describe both friction and wear behavior unless specifically stated as “friction break-in”.

On the Contrary, the steady state in tribology, that condition of a given tribosystem wherein the average kinetic friction coefficient, wear rate, and other specified parameters have reached and maintained a relatively constant level.

Blau [16] summarized eight types of common observed friction break-in curves (Figure 2.1 a-h) He further employs these break-in curves to evaluate the wear and friction mechanisms in the sliding processes.

The coefficient of friction increases monotonically to the steady state in type A (Figure 2.1 a). According to Blau [16], this curve can be explained as the removal of the surface oxides. This friction behavior can also be explained as the work hardening effect, which increases the yield stress at near-surface regions.

Type B friction curve (Figure 2.1 b) [16] features a rapid increasing after the sliding starts, however, followed by a drop in the friction curve. The increase of

coefficient of friction can be also related to work hardening and the removal of oxides layer. The drop in the friction curve is attributed to the crystallographic reorientation in the near-surface regions.

Type C friction curve (Figure 2.1 c) [16] can be interpreted as the combination of a type B break-in curve with a transition to a new steady state following shortly thereafter. Similarly, type D (Figure 2.1 d) [16] has the basic shape of type C except for a higher relative height of the initial peak in the curve. It can be also related to a separate break-in form or as break-in combined with a later transition in steady states.

Type E (Figure 2.1 e) [16] transitions have been observed in the tests of self-lubricating polymers. The break-in curve is followed by a relatively level period and a transition to a higher level of friction. The wear rates often increases after the transition as well.

Type F (Figure 2.1 f) [16] features a relatively high value then decreases monotonically to the steady state. This curve often observed in the sliding of metals in vacuum. This curve suggests a strong effect of surface roughness. This curve is also observed in the re-run-in behavior.

Type G and H friction curve is shown in Figure 2.1 g and Figure 2.1 h [16]. Both of these two types of the friction start with the type F friction curve. Types G and H are relatively uncommon and can be related to the abrasive wear-in and slider grooving followed by self-mated influence to the friction force.

2.4 The applications of PVD TiN, AlTiN and CrN in machining process

2.4.1 Arc vapor deposition process

Arc vapor deposition uses a high current, low voltage arc to vaporize a cathodic electrode (cathodic arc) or anodic electrode (anodic arc) and deposit the vaporized material on a substrate [32]. The vaporized material is highly ionized and usually the substrate is biased so as to accelerate the ions to the substrate surface. Arc vapor deposition is used to deposit hard and decorative coatings. The ions that are formed in arc vaporization are useful in the ion plating process [33].

2.4.2 PVD TiN coatings

Thin wear-resistant hard PVD coatings have been widely applied in cutting tools to enhance their lifetime productivity and performance. TiN is the first generation of PVD hard coating and is now still being widely used as protective hard coatings for bearings, gears, and cutting and forming tools [34]. Due to the advantages of the PVD process such as low deposition temperatures, excellent adhesion strength, relative smooth coating surface, fine-grained and crack-free microstructure, compressive internal residual stress and strong adhesion even on sharp edges [35]. PVD TiN coatings are successfully applied to cemented carbide tools and inserts to improve the performance of interrupted cuttings. The PVD TiN coated tools have been also proved to be superior milling performance due to the enhance abrasion resistance [36]. TiN coatings also provide improvement of wear resistance fatigue strength [37]. Guu et al [38] reported that PVD

TiN coatings can extend tool life to three times compare to uncoated tools. This can be attributed to the improvement of impact strengths, hardness and toughness. Lin et al [39] demonstrated that TiN coated drills with reduced the thrust force and tool wear significantly. It had definitely provided a better cutting ability and a longer tool life.

2.4.3 PVD AlTiN coatings

Since the first application of PVD TiN coatings, a variety range of PVD coatings are employed for machining applications. The main drawbacks for the TiN coatings are the low fracture toughness and oxidation resistance [34]. To address this problem, aluminum were added into TiN coating when deposited as solid solutions. AlTiN were commercialized especially for high speed machining applications, thanks to its physical, chemical, mechanical properties [36]. The cutting performance of AlTiN coated tools performed over TiN coatings especially at high cutting speed, which could be attributed to the solid solution strengthening [40]. When the content of aluminum was further increased, substituting aluminum atoms may improve chemical stability by forming stable Al_2O_3 layer [36]. This Al_2O_3 layer can improve the abrasive wear and crater wear resistance [36]. Palday et al [41] reported that the formation of AlN phase increases hardness in ceramic coatings. The incorporation of aluminum in TiN coatings enhances the oxidation resistance behavior and the thermal stability of the coating [41]. Thus, AlTiN and AlTiN based multilayer coatings show superior performance in applications including machining titanium alloys over the other commercially available Ti based

coatings.

2.4.4 PVD CrN coatings

CrN is a new generation of hard PVD coating. It has been successfully applied to wear resistance components. CrN is also superior to TiN in corrosion resistance, oxidation resistance and fracture toughness [42]. Warcholinski et al [43] reported that CrN coatings exhibit a high hardness and good adhesion, thus are employed in machining from low-alloy steel and high-speed steels. The industrial tests show that an improvement of the cutting edge and rake face performance [43]. Pradhan reported that when depositing CrN film by PVD methods, an increasing of the ion energy can result in increasing the residual stress, thus modify the microstructure of CrN [44]. CrN coatings are widely applied for applications of forming and casting dies, because its wear resistance, low friction coefficient and high Hardness [45]. CrN coatings also demonstrate excellent corrosion resistance properties under severe environmental condition and superior oxidation resistance up to 700°C [34].

2.4.5 The application of PVD coatings in machining titanium alloys

Recent years have seen a huge advancement in the application of carbides, nitrides and polycrystalline diamond coatings in the cutting tools, which influence the machining process. However, the machining speed and material removal speed of titanium alloys are yet to meet the industry requirement. Extensive researches have been done to understand the cutting process and chip formation of titanium alloys.

The coating of tool and dies materials with ceramic based film layers can be conveniently obtained by vapor deposition techniques [46, 47]. Especially, arc vapor deposition technique is the most suitable method for this purpose [47]. Ceramic based coatings provide some advantages, including high micro-hardness, low coefficient of friction, preventing of micro cracks propagation, heat resistance, and excellent corrosion strength [48, 49].

Various surface treatments include the plasma modification, ion implantation, laser modification, and PVD and CVD technologies. The primary surface treatment intends to modify the microstructure of the surface layer and retain its chemical composition by applying rapid heating and cooling rates at high temperature. The secondary surface treatment focuses on the methods of introducing a coating on the bulk material. The tertiary surface treatment considers thermochemical treatment such as nitriding, case carbonizing, and oxidizing on titanium alloys. In the meantime, combinations of various surface treatments draw engineers' attentions in past few decades [50].

The high strength of titanium alloy at elevated temperature and low modulus of elasticity often result in their welding to the cutting tools during machining, therefore, leading to chipping and tool failure [47]. However, the machining titanium at a desired speed without shorten the tool dramatically is still a problem insofar. Tungsten carbide (WC/Co) is so for the most widely applied material in machining titanium alloys because of its balance of cost and performance [51]. All the chemical vapor deposition (CVD)

tested so far has been proved to show a higher wear rate than WC/Co, however, Ezugwu and Pashby [52] pointed out that TiN with fine grains showed improved performance in milling titanium. Carvalh et al. [53] further developed and FEM calculation to evaluate the performance of PVD coated (Ti,Al,Si)N. The strong chemical reaction tendency of titanium alloys often result in a poor surface finish after machining and milling. Wang [47] tested TiN, TiAlN and CrN coatings for die materials and showed that TiAlN and CrN coatings are appropriate coating materials because of their high corrosion resistance. Dobrzanski et al [54] obtained the best wear resistance in TiN coating both at room temperature and at 500°C test temperature condition.

Table 2.1 Mechanical properties of TI-10V-2FE-3AL and TI-6AL-4V [4]

	TI-10V-2FE-3AL (ST 760°C + AGED 385°C)	TI-6AL-4V ELI (GRADE 23),ANNEALED
DENSITY	4.65 G/CC	4.43 G/CC
MECHANICAL PROPERTIES		
HARDNESS, VICKERS	475	341
TENSILE STRENGTH, ULTIMATE	1430 MPA	860 MPA
TENSILE STRENGTH, YIELD	1240 MPA	790 MPA
COMPRESSIVE YIELD STRENGTH	1280 MPA	860 MPA
FATIGUE STRENGTH (KT =3.0)	450 MPA @ # OF CYCLES 1.00E + 7	140 MPA @ # OF CYCLES 1.00E + 7
SHEAR STRENTH	760 MPA	550 MPA
FRACTURE TOUGHNESS	131.2 MPA M1/2	100 MPA M1/2

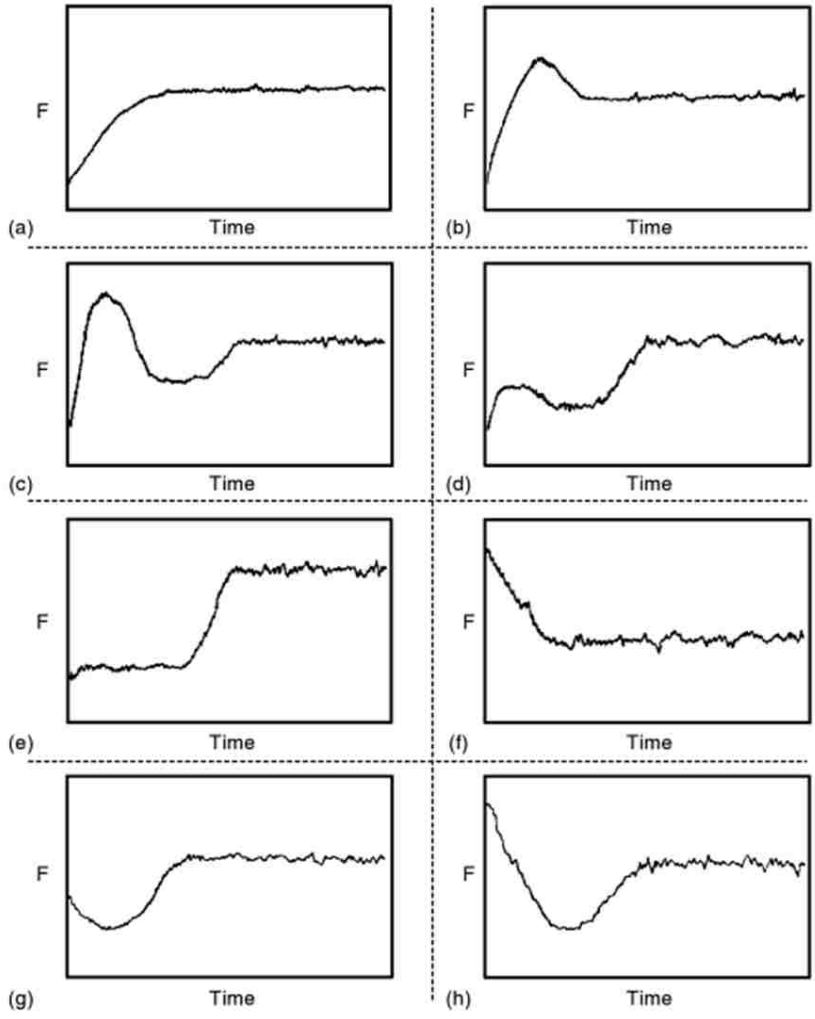

Figure 2.1 The typical friction behavior (friction force v.s. time) of break-in period [55]

CHAPTER 3 MATERIALS AND EXPERIMENTAL METHODS

3.1 Overview

The wear and adhesion behaviors of Ti-6Al-4V are studied in this chapter. The wear tests were performed using a CETR UMT multi-specimen test system with a ball-on-disc test apparatus. The adhesion tests were performed using the same CETR UMT multi-specimen test system with a ball-on-flat test apparatus. The surfaces of both ball samples and disks samples were observed by Veeco optical profiler (WYKO) to investigate the surface roughness both before and after the tests. Scanning electron microscopy (SEM) was employed to study the wear mechanisms of different combinations of Ti-6Al-4V to different counterface materials. Elemental analysis of the microstructural features were performed using electron energy loss spectroscopy (EELS) and EDS microanalysis and structural information and phase identifications of the transferred materials were performed with high-resolution TEM (HRTEM) imaging and corresponding fast Fourier transform (FFT) patterns as well as convergent beam electron diffraction (CBED) patterns. The TEM samples were prepared using the FIB lift-out technique.

3.2 Materials

3.2.1 Ti-6Al-4V Titanium alloy

Ti-6Al-4V alloy used in this research was received in the mill-annealed condition with an equiaxed microstructure consisting of primary α grains and β particles at α grain

boundary (Figure 3.1). The alloy had an average hardness of 350 ± 6 $HV_{0.05}$, measured according to ASTM E384 standard using a Buehler Micromet II microhardness tester at an applied load of 50 grf (0.49 N) and an elastic modulus of 114 GPa [4]. The Ti-6Al-4V discs have a 25 mm diameter and 5 mm thickness. The titanium disks were polished to an average surface roughness (R_a) of 25±5 nm (measured using optical profilometry) by the conventional metallographic procedure for titanium alloys. This conventional metallographic procedure for Ti-6Al-4V insured that the effect of the surface roughness of titanium surfaces can be neglected. The titanium disks were also numbered to document the test result. The samples were ultrasonic cleaned in ethanol.

3.2.2 Nitride coatings

The counterface materials were 12 mm-diameter AISI 52100 steel balls coated with AlTiN, TiN and CrN coatings. Figure 3.2 shows the images of three different nitride coatings tested in this experiment. The AlTiN coating had a thickness of 3.5±0.2 μm, the TiN coating has a thickness of 4.0±0.2 and the CrN coating had a thickness of 4.5±0.2 μm. All the coatings were deposited in a commercially available cathodic arc physical vapor deposition (PVD) system[1]. In order to minimize the effect of initial surface topography on the adhesion and friction behavior, the counterface balls were mechanically polished with 3 μm diamond followed by 1 μm diamond on short napped

[1] Ionbond US -Madison Heights, 1823 East Whitcomb, Madison Heights, USA MI 48071

polishing cloth to an average surface roughness (R_a) of 58.3±6.8 nm (measured by optical profilometry). The details of properties and roughness of the counterface balls are summarized in Table 3.1. The ball samples were ultrasonically cleaned in an ethanol bath and dried before the experiments.

3.3 Wear and adhesion tests

The ball-on-disk tests were carried out at 3 N load, 0.167 mm/s speed for a total sliding distance of 10 m (200 cycles) using Bruker's UMT tribometer (Figure 3.3). The amount of wear of Ti-6Al-4V disks was determined by weight measurements before and after each test using a Sartorius LE225D electronic balance to the precision of 0.1 mg and wear rates were obtained by dividing mass loss by the total sliding distance. The adhesion tests were also conducted for a sliding distance of 0.01 m at the same sliding speed (0.167 mm/s) and normal load (3 N load) as the ball-on-disk tests to investigate adhesion behavior of Ti-6Al-4V to difference counterface materials.

All the tests were performed in ambient conditions at 25˚C and 40% relative humidity. Each test was repeated and the reported wear rates were the average values obtained from three tests. Real-time dynamic load and tangential force values were recorded during the tests and the coefficient of friction (COF) values were calculated accordingly. The tests were also conducted against an uncoated AISI 52100 steel ball under the same conditions, for the purpose of comparison.

3.4 Surface analysis

3.4.1 Surface morphology

The surface roughness of samples was measured using a Veeco Wyko NT1100 optical profiling system. The Veeco Wyko NT1100 is an optical profiler providing three-dimensional surface profile measurements without contact. The phase shift interference (PSI) mode, based on optical phase-shifting, is dedicated to roughness measurements with a maximum 150 nm peak-to-valley topography. The volume of transferred titanium alloy after the adhesion tests was also measured by optical profiling system. Figure 3.3 shows the Veeco Wyko NT1100 optical profiler at the Tribological Research Center at the University of Windsor.

3.4.2 Scanning electron microscopy analysis

An FEI Quanta 200 FEG scanning electron microscope (SEM) equipped with an energy-dispersive X-ray spectroscopy (EDS) system (Figure 3.4) was used to observe both titanium disk and counterface ball surfaces after the wear tests. Plain views of the wear tracks and wear debris were observed to identify the morphology of the worn surface under each loading condition. EDS was used to determine quantitatively the composition of the wear debris and selected locations on the wear tracks.

3.4.3 Transmission electron microscopy and focused ion beam techniques

A dual beam Zeiss NVision 40 equipped with a focused ion beam (FIB) milling instrument and a field emission gun (FEG) scanning electron microscope (SEM) was

employed for cross-sectional examination and imaging of the microstructure of titanium transfer layers and their adhesion to the counterface balls. Prior to the milling process, a thin (2 μm) tungsten layer was deposited on the surface at regions of interest to minimize the damage during the milling process. Detailed investigation of the microstructure of the transfer layers specifically at the interface region with different counterface surfaces were carried out using a FEI Titan 80-3000 scanning electron microscope (SEM) and transmission electron microscope (TEM). Elemental analysis of the microstructural features were performed using electron energy loss spectroscopy (EELS) and EDS microanalysis and structural information and phase identifications were performed with high-resolution TEM (HRTEM) imaging and corresponding fast Fourier transform (FFT) patterns as well as convergent beam electron diffraction (CBED) patterns. The TEM samples were prepared using the FIB lift-out technique.

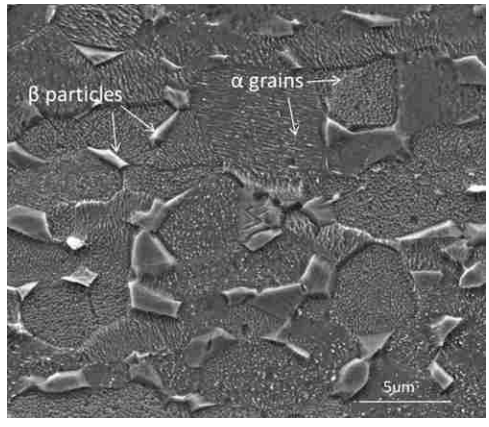

Figure 3.1 Secondary electron SEM image of the microstructure of the as-received Ti-6Al-4V alloy used in this investigation (etched in Kroll's). The alloy had a "mill-annealed" microstructure consisting of primary equiaxed α grains and grain boundary β particles

AlTiN TiN CrN

Figure 3.2 Photography images of PVD coatings

Figure 3.3 WYKO optical profiling microscopy including the full Wyko Vision® analytical software package

Figure 3.4 Scanning electron microscopy employed in research objective from Great Lakes Institute for Environmental Research at University of Windsor

Table 3.1 Properties of counterface material used in this investigation

Counterface	Hardness ($HV_{0.05}$)	Thickness (μm)	Average surface roughness, R_a (nm)	Chemical composition	Crystal structure
AlTiN coating	~ 3500	3.5 ± 0.2	60.6 ± 4.5	$Al_{0.67}Ti_{0.33}N$	AlTiN (FCC) + AlN (Hexagonal)
TiN coating	~ 2400	4.5 ± 0.2	81.6 ± 6.0	TiN	FCC
CrN coating	~ 2300	4.5 ± 0.2	63.6 ± 6.0	CrN	Orthorhombic
AISI 52100 steel	800	-	50.6 ± 4.0	-	-

CHAPTER 4 EXPERIMENTAL RESULTS

4.1 Overview

The characterizations of the Ti-6Al-4V, including microstructure surface morphology, adhesion and wear properties, are demonstrated in this chapter. The coefficient of friction of both ball-on-disk wear tests and adhsion tests with different counterface materials to Ti-6Al-4V are shown in this chapter. Surface roughness measurements, the cross-sectional microstructure and diffraction patterns are presented to explain the adhesion mechanisms of Ti-6Al-4V to different counterface materials. The worn and slided surfaces are observed using SEM. Wear tracks and wear debris after wear testing are analyzed.

4.2 Wear and adhesion behaviors of Ti-6Al-4V

4.2.1 Microstructure of as-received Ti-6Al-4V and surface roughness

Ti-6Al-4V specimens had a homogeneous structure perpendicular and parallel to the rolling direction. Ti-6Al-4V alloy used in this research was received in the mill-annealed condition with an equiaxed microstructure consisting of primary α grains and β particles at α grain boundary. The average surface roughness (Ra) the titanium alloys was 25±5 nm.

4.2.2 Ball-on-disk tests of Ti-6Al-4V alloy

Variations of wear rates with different counterface materials of Ti-6Al-4V in 10 meter ball-on-disk tests with 3 N applied load are plotted in Figure 4.1. The wear rate of

Ti-6Al-4V disks against different counterface materials after the ball-on-disk tests determined from mass loss measurements. Similar values of wear rate were obtained when Ti-6Al-4V sliding against steel CrN, TiN and AlTiN; however, slightly lower wear rate was obtained against CrN. Figure 4.2 shows the sliding track morphologies on the surface of Ti-6Al-4V disks after the ball-on-disk tests against different counterface materials (steel, CrN, TiN, and AlTiN). It can be observed that Ti-6Al-4V experienced severe damage after 10-meter sliding tests against all the tested counterface materials. The sliding tracks consisted of ploughing marks and debris. Three types of debris morphologies were observed as shown in Figure 4.3; large plate-like particles (Figure 4.3 a), cutting chip-like debris (Figure 4.3 b), and equiaxed fine particles (Figure 4.3 c). The EDS analyses of the wear debris particles revealed the presence of titanium, aluminum, vanadium, and oxygen. However, higher oxygen content was found in the fine wear debris particles (Figure 4.4).

Figure 4.5 presents back-scattered electron SEM images of the counterface balls showing transfer of material to the counterface surfaces after the ball-on-disk tests. The EDS analyses demonstrated that the observed transferred material contained titanium, aluminum, vanadium and oxygen.

4.2.3 Adhesion tests of Ti-6Al-4V alloy

The contact surfaces of the counterface balls after adhesion tests are presented in the three-dimensional (3D) optical profilometry images in Figure 4.6 showing transfer of

material to the counterface after sliding distance of 0.01 m. The volume of transferred Ti-6Al-4V measured based on the corresponding optical profilometry images is shown in Figure 4.7. It is observed that the transferred material to the CrN is the least compared to the other three counterface materials.

Figure 4.8 exhibits back-scattered electron SEM images of the transferred material to the counterface balls after the adhesion tests (applied load: 3 N, sliding distance: 0.01 m) showing that significant material transfer occurred during the tests, however, no significant loose debris particles were generated after the tests. The EDS analysis indicated that the materials transferred to the ball counterfaces are composed of titanium, aluminum, vanadium, and oxygen.

Analytical microscopy observations reveal no evidence of spallation or failures inside the coatings or at the interface between the coatings and steel substrates after the tests. Back-scattered electron SEM images of the FIB-milled cross section of the transferred material the counterface balls are shown in Figure 4.8. Strong adhesion is observed between the transfer layer/steel (Figure 4.9) showing a transfer layer/steel and transfer layer/AlTiN (Figure 4.9 b) counterface surfaces. However, a lateral microcrack is observed at the interface between the transfer layer and the TiN coating (marked by an arrow in Figure 4.9 c). Similar lateral microcrack is observed at the interface between the transfer layer and CrN coating (marked by an arrow in Figure 4.9 d).

The variation of coefficient of friction (COF) with sliding distance of Ti-6Al-4V

surfaces against different counterface materials during adhesion tests are shown in Figure 4.10. The initial stages of sliding, during which COF increased abruptly, have been also marked on the image. It is observed that for the Ti-6Al-4V/CrN sliding pair the COF value reached a more stable condition after a short sliding distance of 0.2 mm, however, the initial stages of sliding for Ti-6Al-4V against steel and AlTiN surfaces are 2 mm and 3.5 mm, respectively. With the continuation of sliding, CrN and AlTiN showed similar friction behavior and the average COF value of the steel counterface was found to be the lowest. Detailed friction results of adhesion tests are summarized in Table 4.1.

In Figure 4.11 the scanning transmission electron microscopy (STEM) images and convergent beam electron diffraction (CBED) patterns were used for characterization of transfer layers after adhesion sliding tests. The results indicates that the microstructure of the transfer layer on all of the counterface balls have a lamellar structure consisting of nanocrystalline (ring diffraction patterns) and polycrystalline (“Spotty” diffraction patterns) regions embedded in an amorphous matrix (diffuse ring diffraction patterns).

The electron energy loss spectroscopy (EELS) maps constructed from the cross section of transfer layers (Figure 4.12) confirm that the transferred material is consisted of layers composed of Ti, V, Al, and O. The electron diffraction patterns taken from several different locations within the transfer layers (Figure 4.13) indicates that regions with a higher oxygen content, contains titanium oxide (TiO, space group C2/m) and vanadium oxide (V_2O_3, C2/c space group).

High-resolution TEM (HRTEM) images and the fast Fourier transform (FFT) patterns at the transfer layer interface with different counterface materials are shown in Figure 4.14. The results are consistent with those of the STEM/electron diffraction patterns (Figure 4.11). A nanocrystalline structure of TiO (ring patterns) is detected at the interface of the transfer layer with steel and AlTiN counterface materials. However, an ultrafine structure (spotty diffraction pattern) of α-titanium was detected at the CrN/transfer layer and TiN/transfer layer interface.

Table 4.1 The friction results and transfer volume of Ti-6Al-4V to different counterface materials

Counterface material	AISI 52100 steel		
Titanium disk number	1	2	3
Averaged steady state COF	0.29	0.27	0.26
Distance to reach Threshold (mm)	2.4	1.7	1.8
Volume transfer (10^{-10} m^3)	0.138	0.137	0.137

Counterface material	AlTiN		
Titanium disk number	1	2	3
Averaged steady state COF	0.37	0.39	0.40
Distance to reach Threshold (mm)	4.3	3.9	3.8
Volume transfer (10^{-10} m^3)	0.138	0.137	0.137

Counterface material	TiN		
Titanium disk number	1	2	3
Averaged steady state COF	0.30	0.26	0.29
Distance to reach Threshold (mm)	0.77	0.80	0.69
Volume transfer (10^{-10} m^3)	0.124	0.123	0.124

Counterface material	CrN		
Titanium disk number	1	2	3
Averaged steady state COF	0.35	0.36	0.38
Distance to reach Threshold (mm)	0.22	0.21	0.17
Volume transfer (10^{-10} m^3)	0.123	0.123	0.122

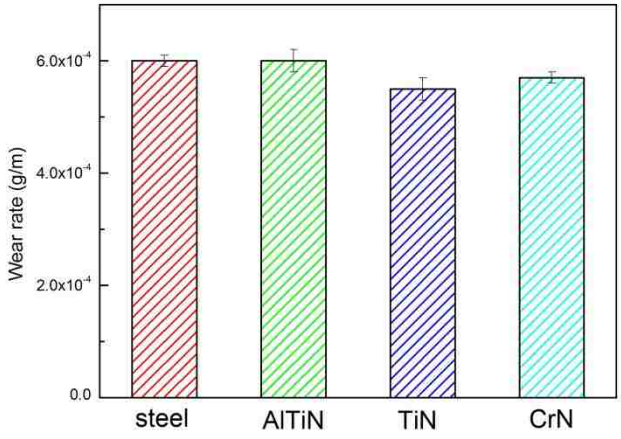

Figure 4.1 Wear rates (mg/m) of Ti-6Al-4V disks against different counterface balls after ball-on-disk tests (applied load: 3 N, sliding distance: 10 m). The wear rates were determined in terms of mass loss by measuring the Ti-6Al-4V test coupons before and after each test

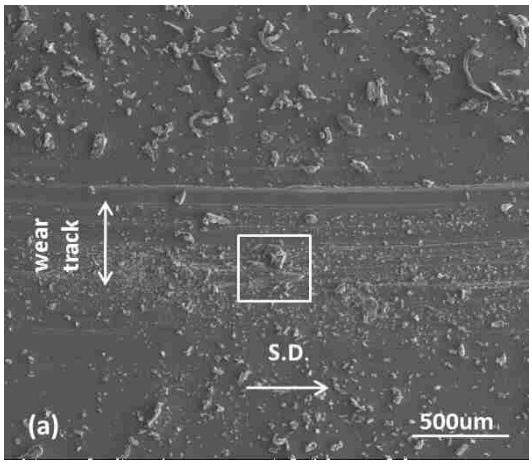
wear
track
S.D.
(a)
500um

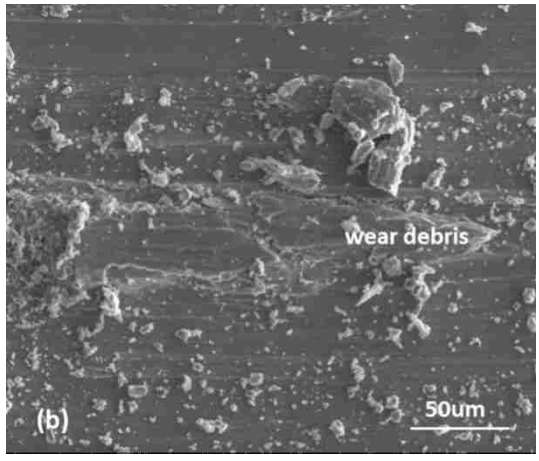
wear debris
(b)
50um

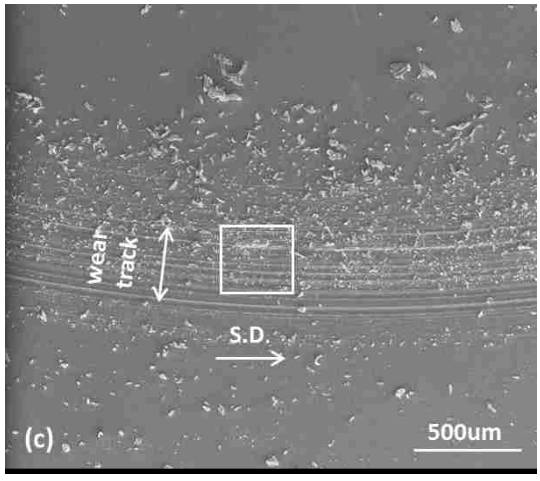
wear
track
S.D.
(c)
500um

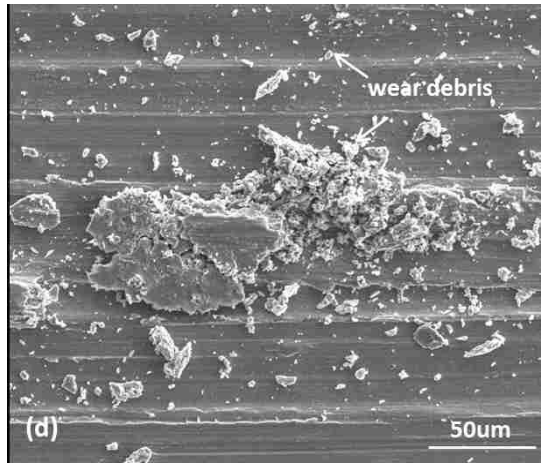
wear debris
(d)
50um

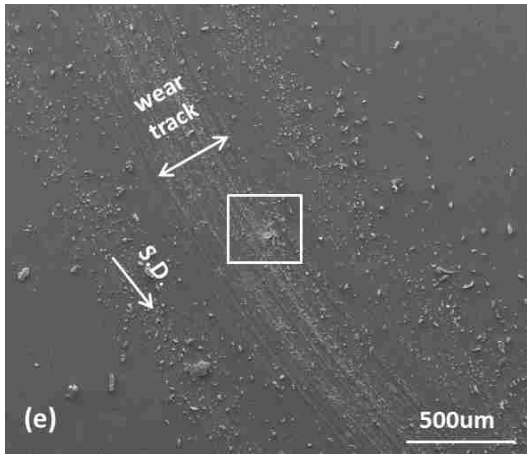
wear
track
S.D.
(e)
500um

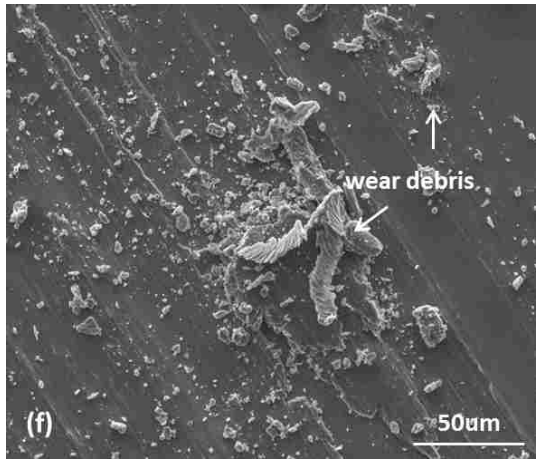
wear debris
(f)
50um

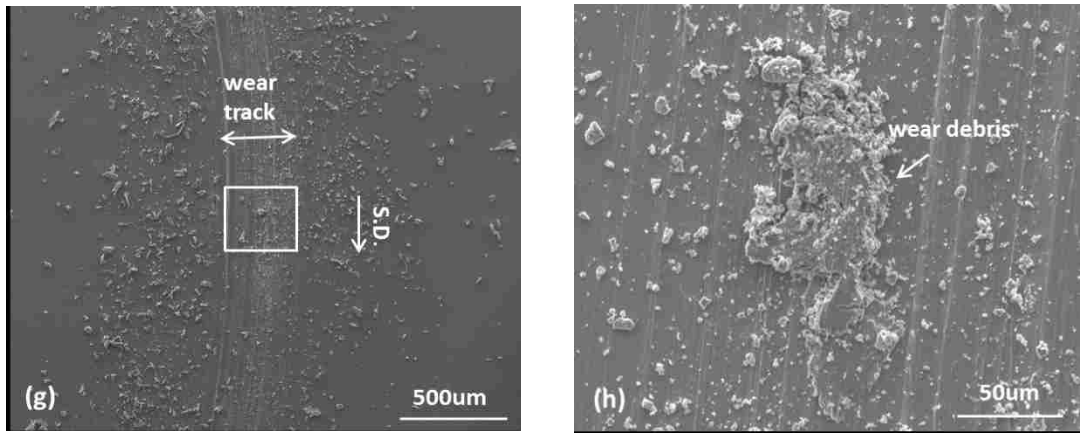

Figure 4.2 Secondary electron SEM images of the wear tracks on the surface of Ti-6Al-4V alloy after ball-on-disk wear tests against (a) steel, (c) AlTiN, and (e)TiN, (g) CrN counterface balls (applied load: 3 N, sliding distance: 10 m). (b), (d), (f) and (h) are higher magnification images of the enclosed areas in (a), (c) and (e) showing the presence of abrasion grooves and wear debris particles on the wear tracks

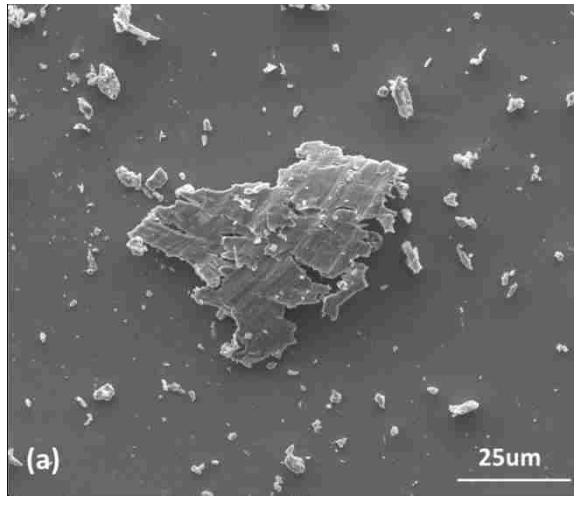

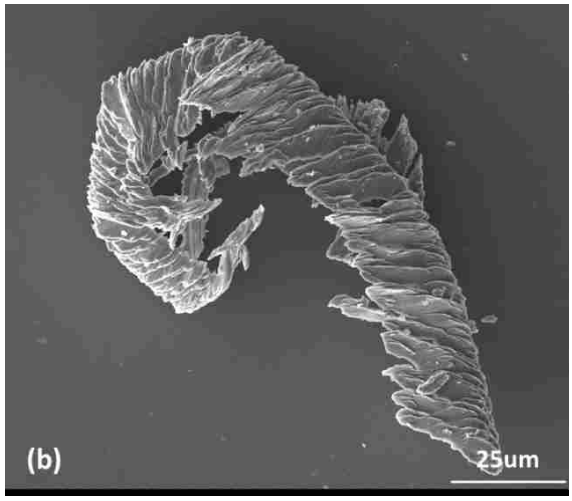

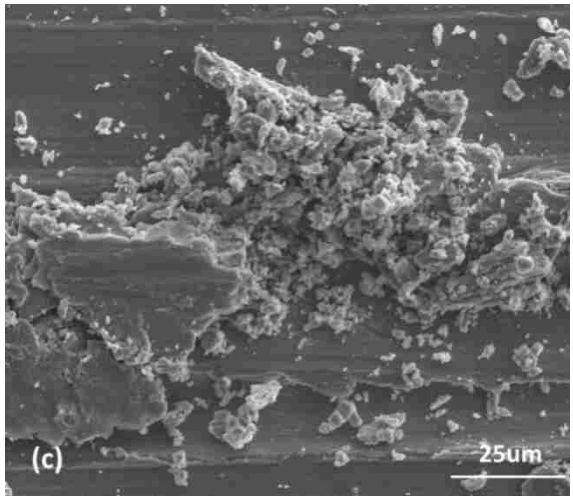

Figure 4.3 Secondary electron SEM images of the different morphologies of wear debris particles found on the wear tracks after ball-on-disk wear tests, (a) large plate-like particles, (b) cutting chip-like debris, (c) fine equiaxed wear particles (applied load: 3 N, sliding distance: 10 m)

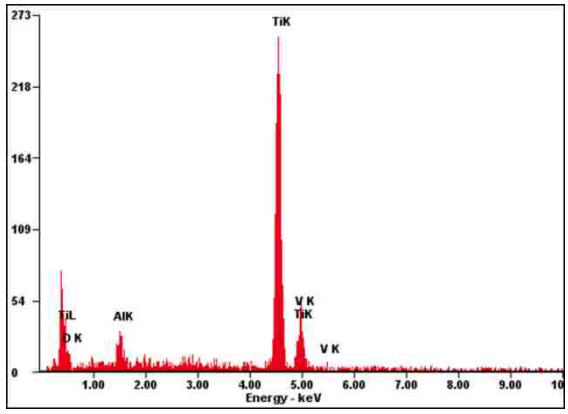

Figure 4.4 EDS spectrum indicates presence of Ti, Al, V. O in the wear tracks

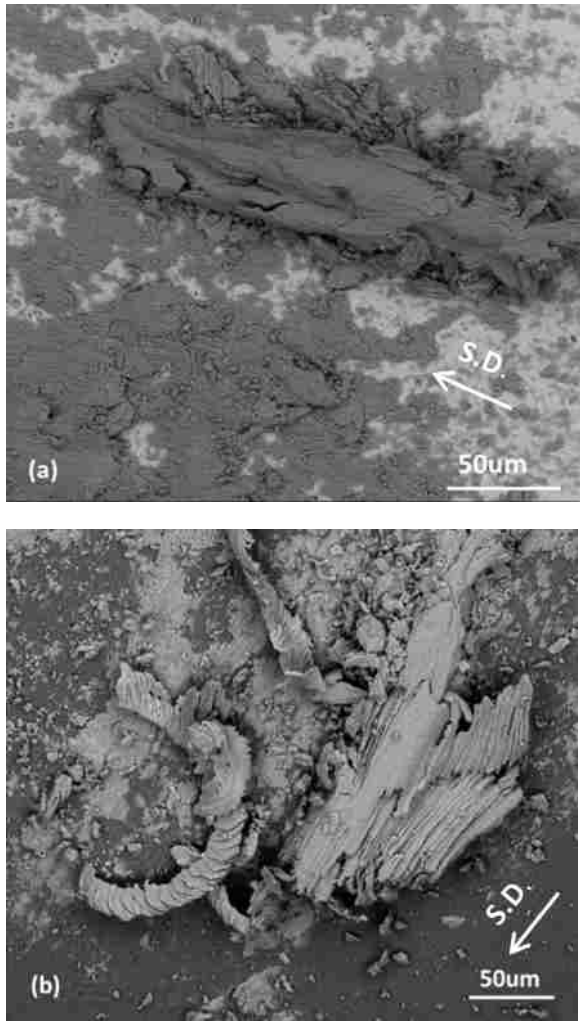

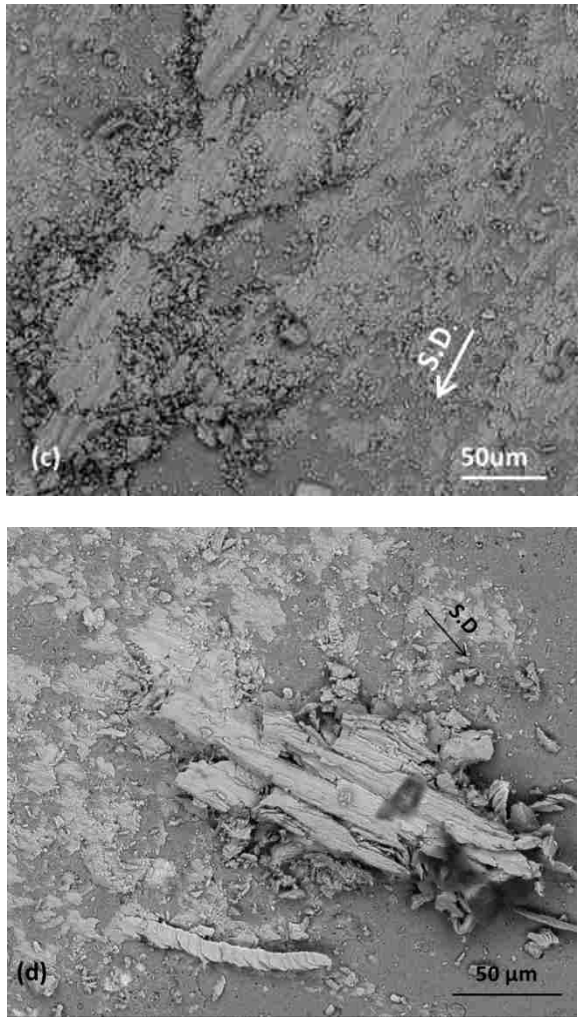

Figure 4.5 Back-scattered electron SEM image of the wear scars on (a) steel, (b) AlTiN, (c) TiN and (d) CrN counterface balls after ball-on-disk tests (applied load: 3 N, sliding distance: 10 m).The EDS analyses indicated that the transferred material observed on the wear scars consisted of Ti, Al, V and O elements

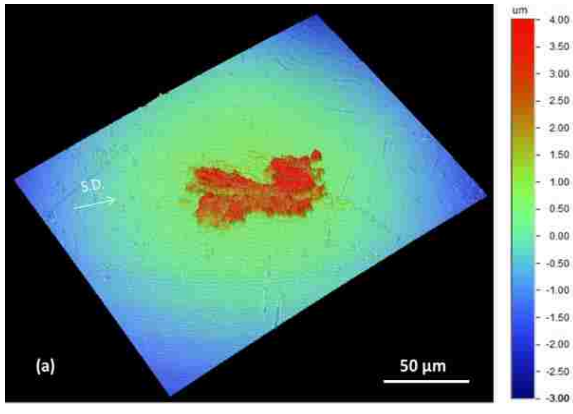

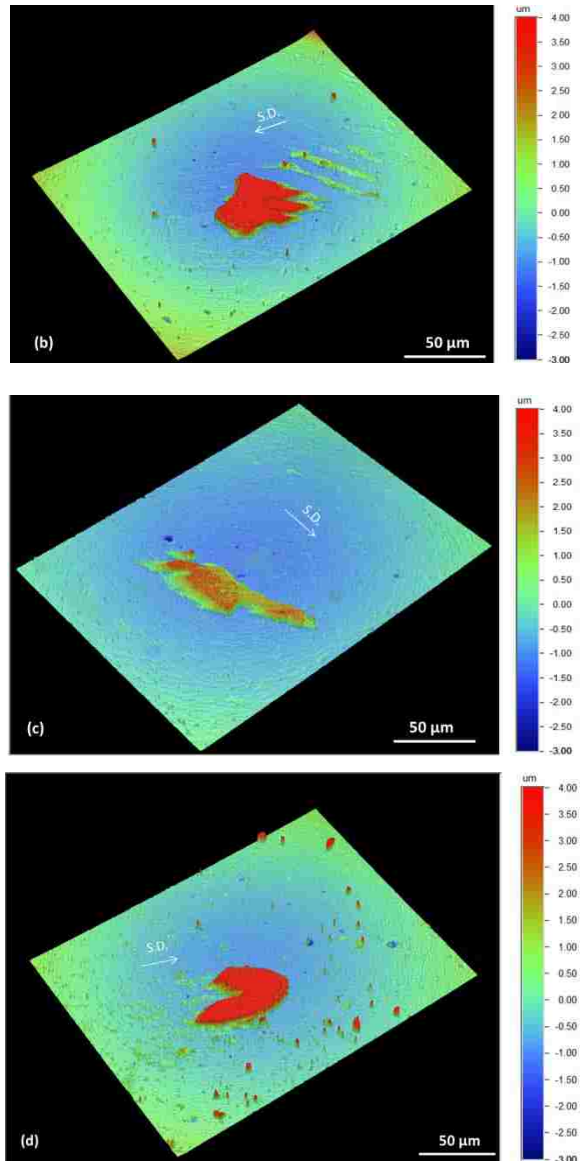

Figure 4.6 3D optical profilometry images showing the wear scars on (a) steel, (b) AlTiN, (c) TiN, (d)CrN counterface balls after ball-on-disk wear tests (applied load: 3 N, sliding distance: 10 m). The EDS analyses indicate

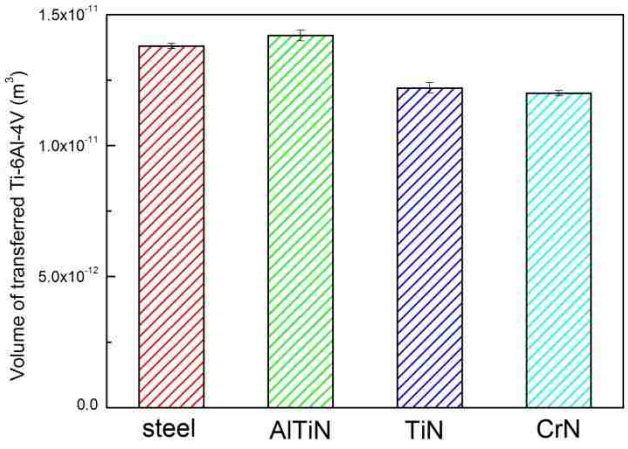

Figure 4.7 The volume of transferred Ti-6Al-4V to different counterface materials after adhesion tests (applied load: 3 N, sliding distance: 0.01 m). The measurements were based on optical profilometry images from the wear scars on the counterface balls

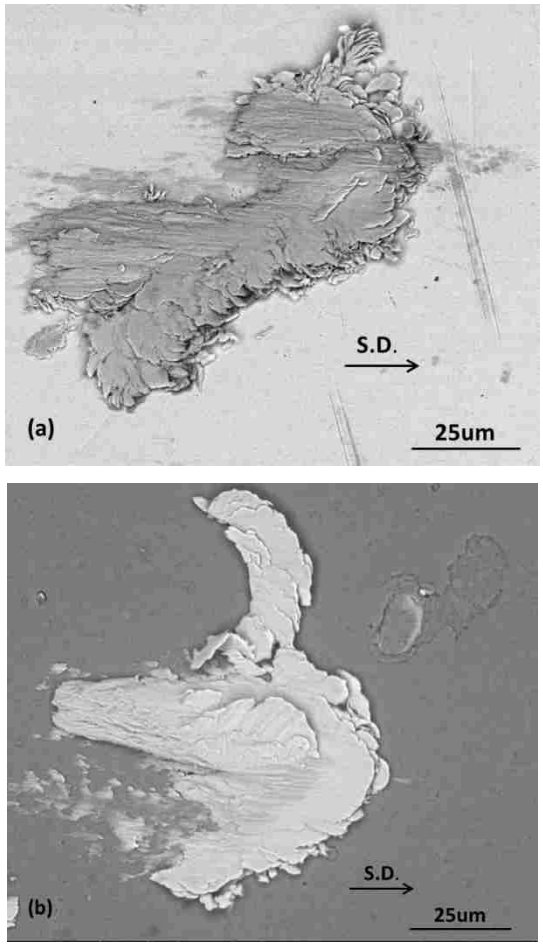

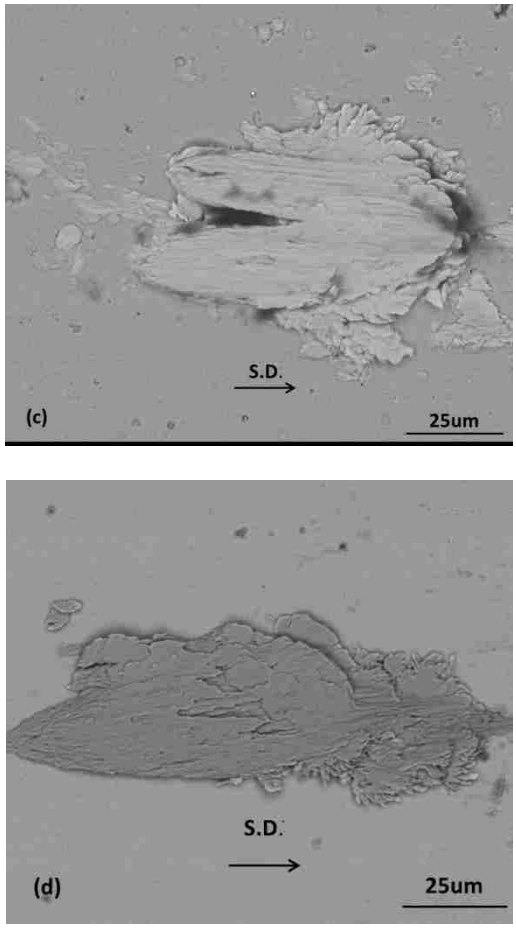

Figure 4.8 Back-scattered electron SEM images images showing the wear scars on (a) steel, (b) AlTiN, (c) TiN, (d) CrN counterface balls after ball-on-disk wear tests (applied load: 3 N, sliding distance: 10 m). The EDS analyses indicate

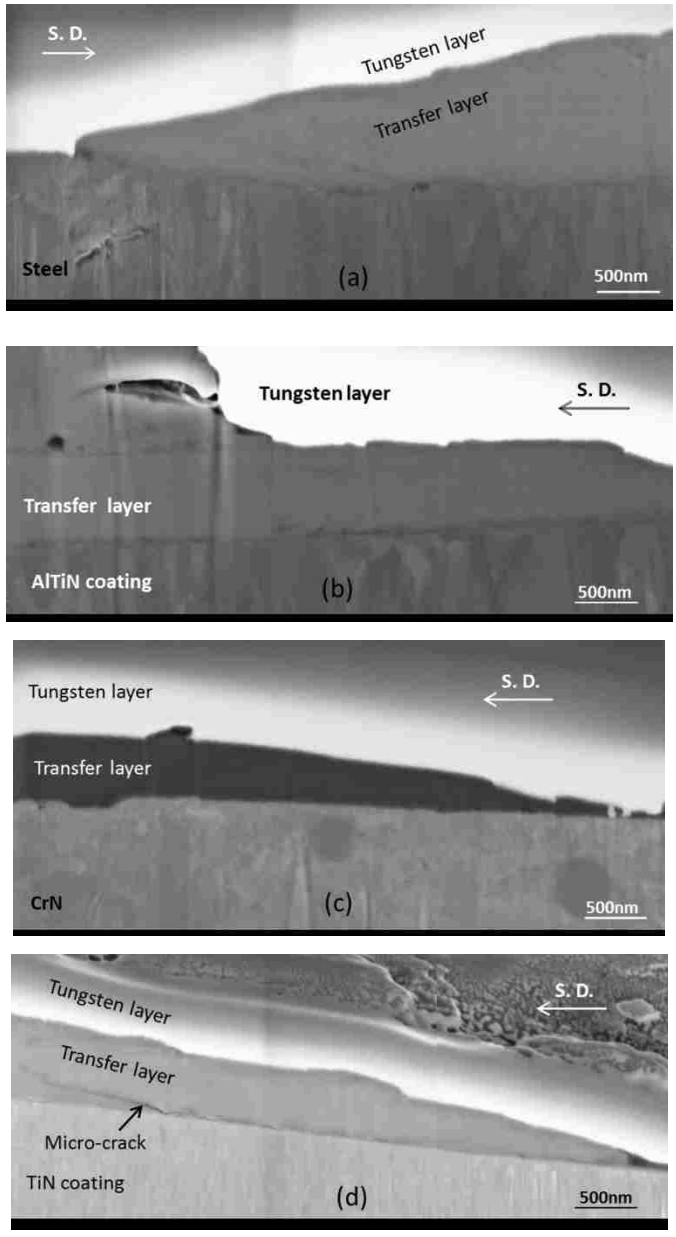

Figure 4.9 Back-scattered electron SEM images of the focused ion beam (FIB)-milled cross sections of transferred Ti-6Al-4V to (a) steel, (b) AlTiN, (c) TiN and (d) CrN counterface balls after adhesion tests (applied load: 3 N, sliding distance: 0.01 m). The sliding direction (S.D.) has been marked on the images

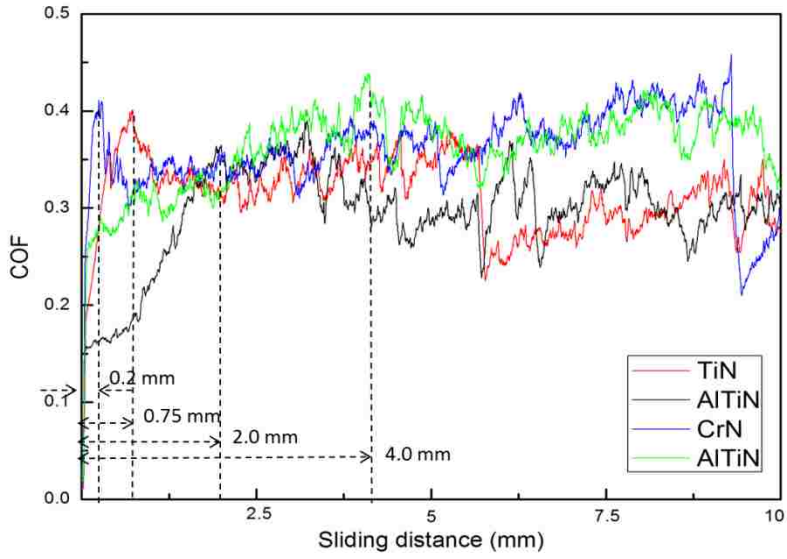

Figure 4.10 Variation of coefficient of friction (COF) with sliding distance during adhesion tests. It was observed that TiN and CrN coating reached a more stable condition after a shorter sliding distance compared to steel and AlTiN coating

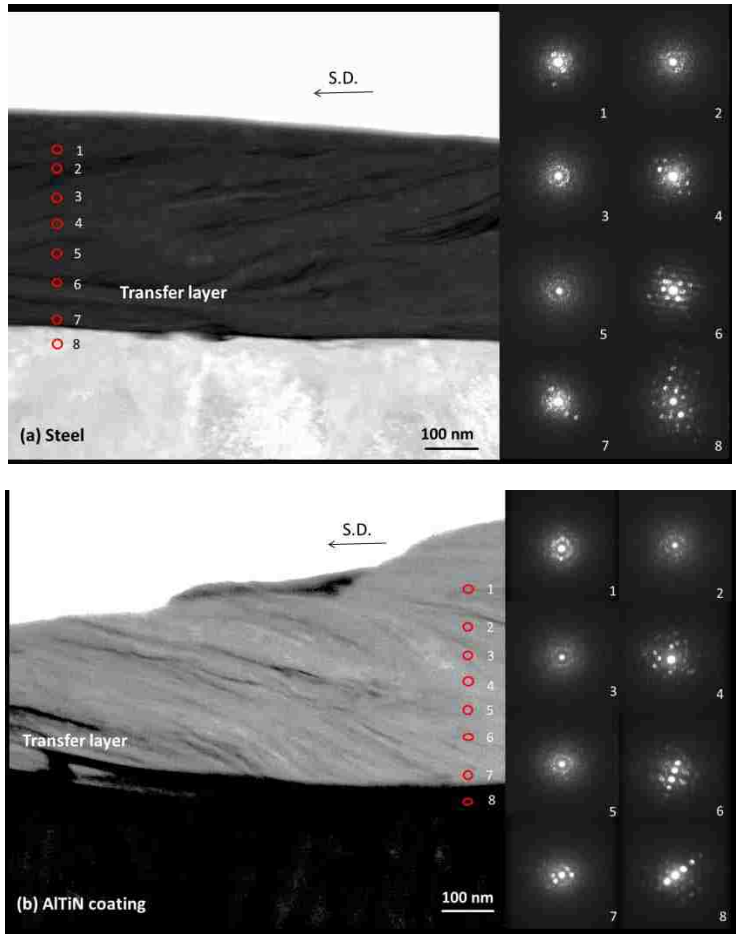

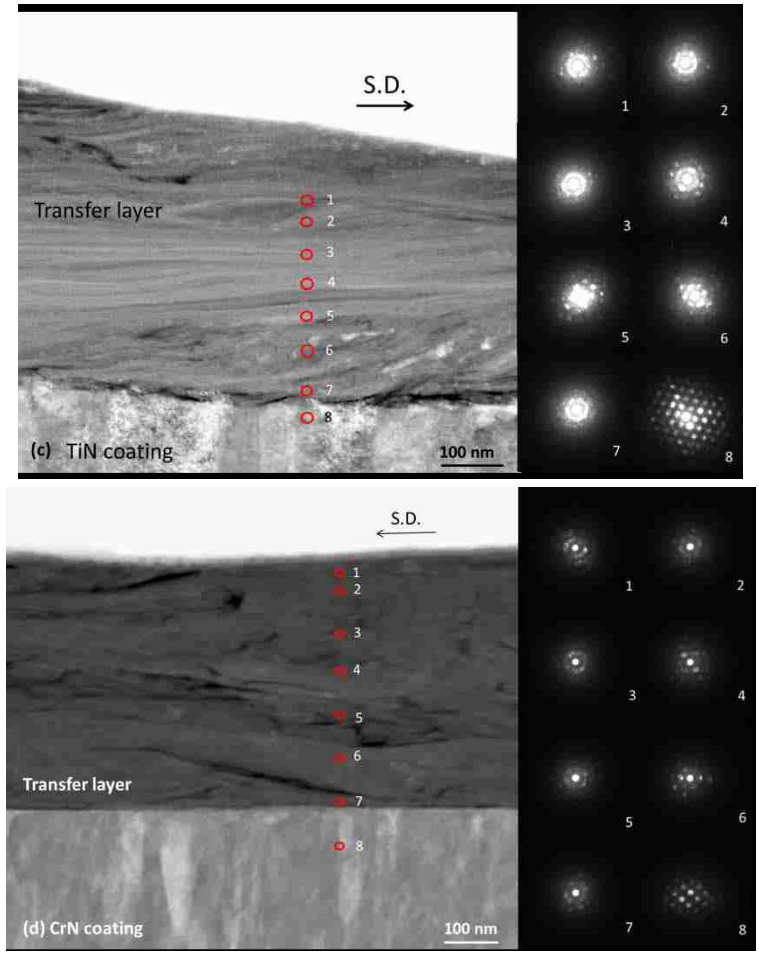

Figure 4.11 Scanning transmission electron microscopy (STEM) images of the cross section of transfer layer and convergent beam electron diffraction (CBED) patterns taken from several locations across the transfer layer (marked on the images) for (a) steel, (b) AlTiN, (c) TiN, and (d) CrN counterface balls. (adhesion tests, applied load: 3 N, sliding distance: 0.01 m). It was observed that the microstructure of the transfer layer consisted of polycrystalline (spotty diffraction patterns) and nanocrystalline (ring diffraction patterns) regions incorporated in an amorphous matrix (diffuse ring diffraction patterns). The sliding direction (S.D.) has been marked on the images

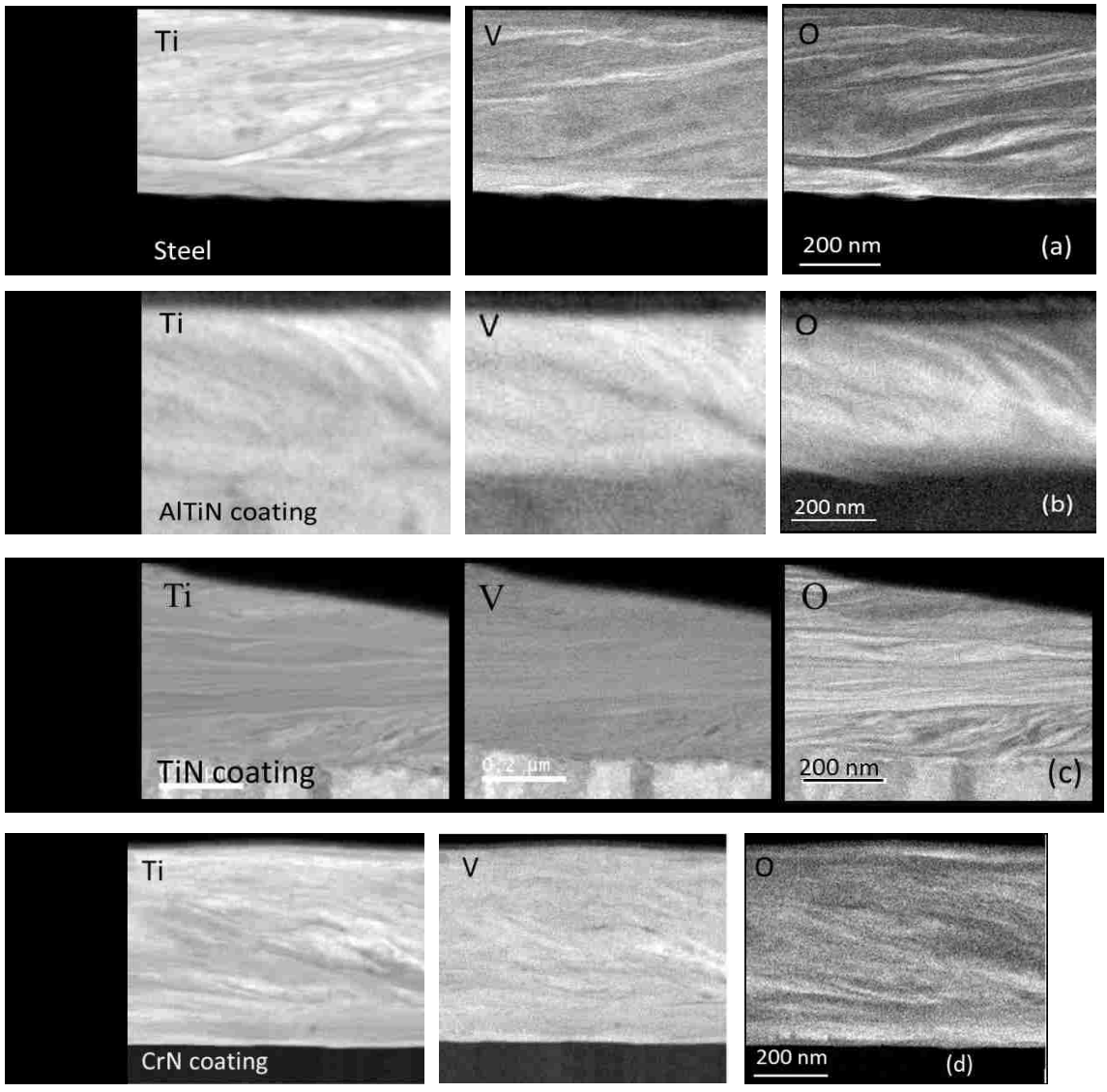

Figure 4.12 Electron energy loss spectroscopy (EELS) maps of the cross section of transfer layers to the (a) steel, (b) AlTiN, (c) TiN and (d) CrN counterface balls after adhesion tests showing the lamellar microstructure of the transfer layers consisting of oxygen titanium and vanadium. (Applied load: 3 N, sliding distance: 0.01 m)

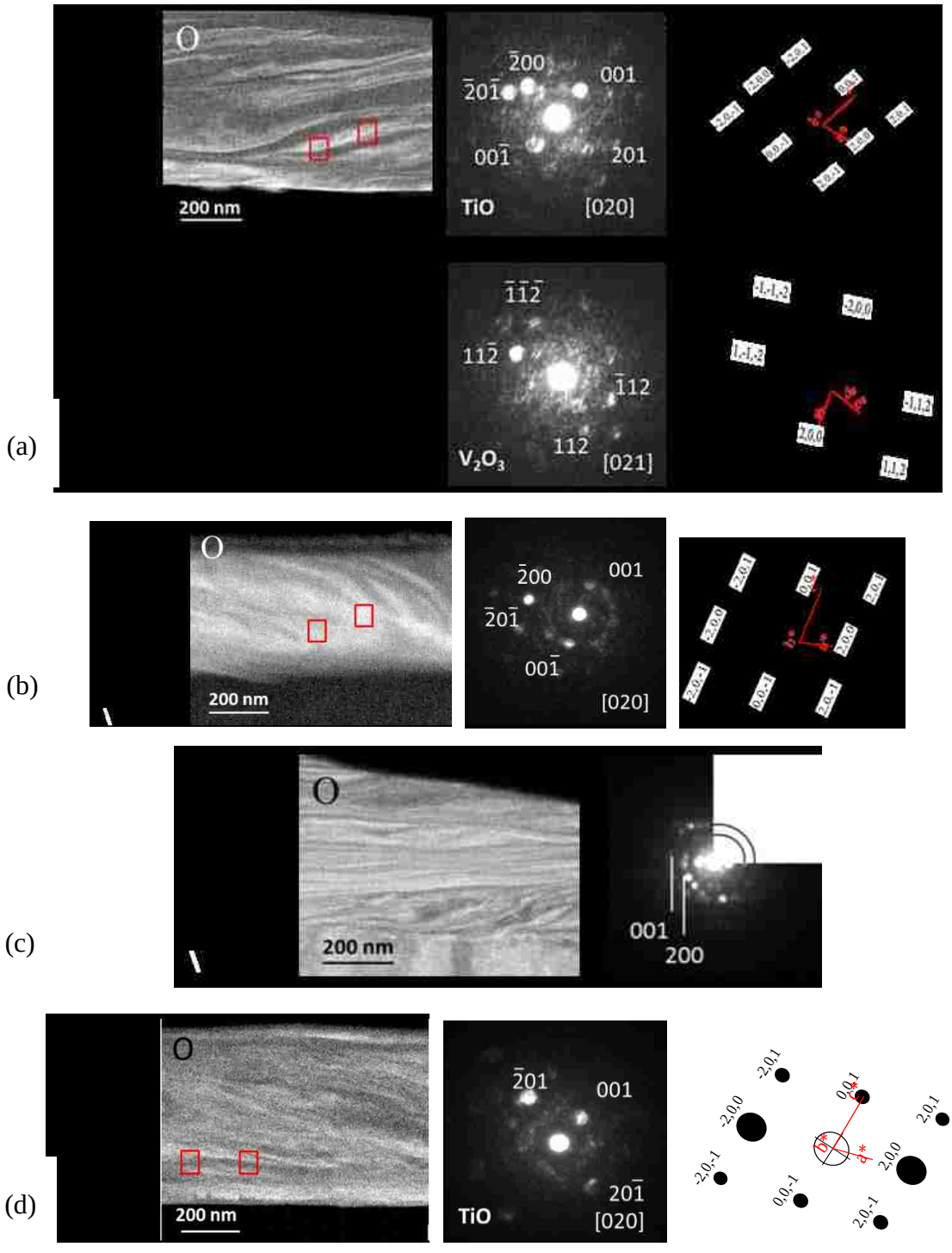

Figure 4.13 Electron energy loss spectroscopy (EELS) maps of the cross section of transfer layers and the corresponding convergent beam electron diffraction (CBED) patterns for the steel, AlTiN, TiN and CrN counterface balls after adhesion tests. The enclosed areas are the locations where CBED patterns were taken. It was observed that TiO (C2/m space group) and V2O3 (C2/c space group) were present in the transfer layer within the regions that had a higher oxygen content

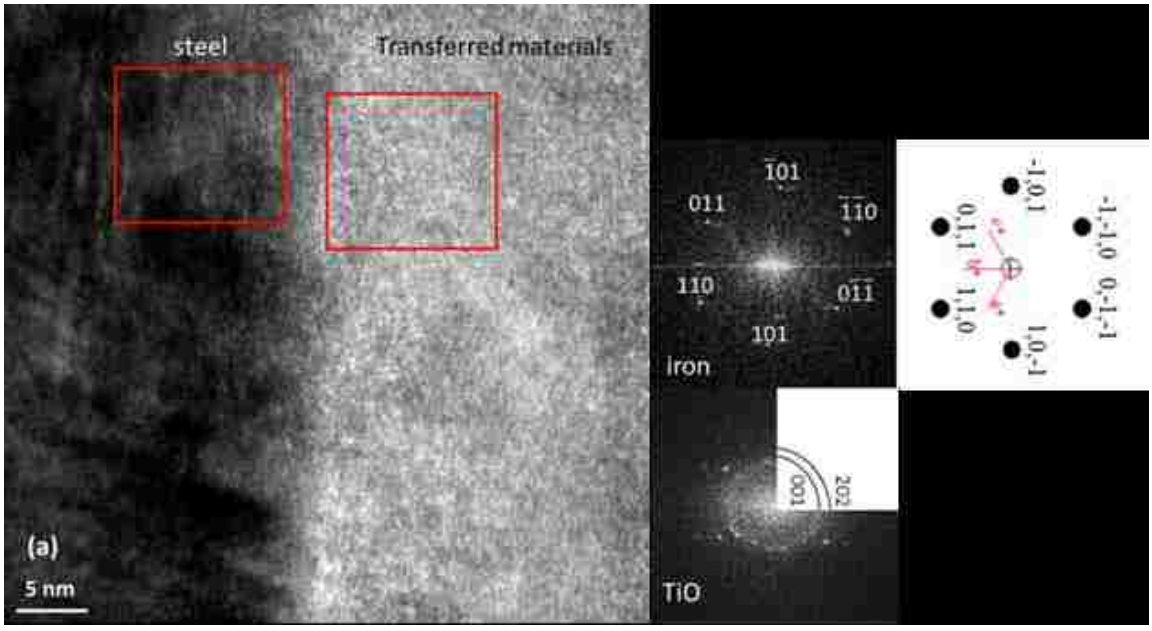
steel
Transferred materials
(a)
5 nm
iron
TiO
-1,0,1
-1,-1,0
0,-1,-1
0,1,1
1,1,0
1,0,-1
001
202

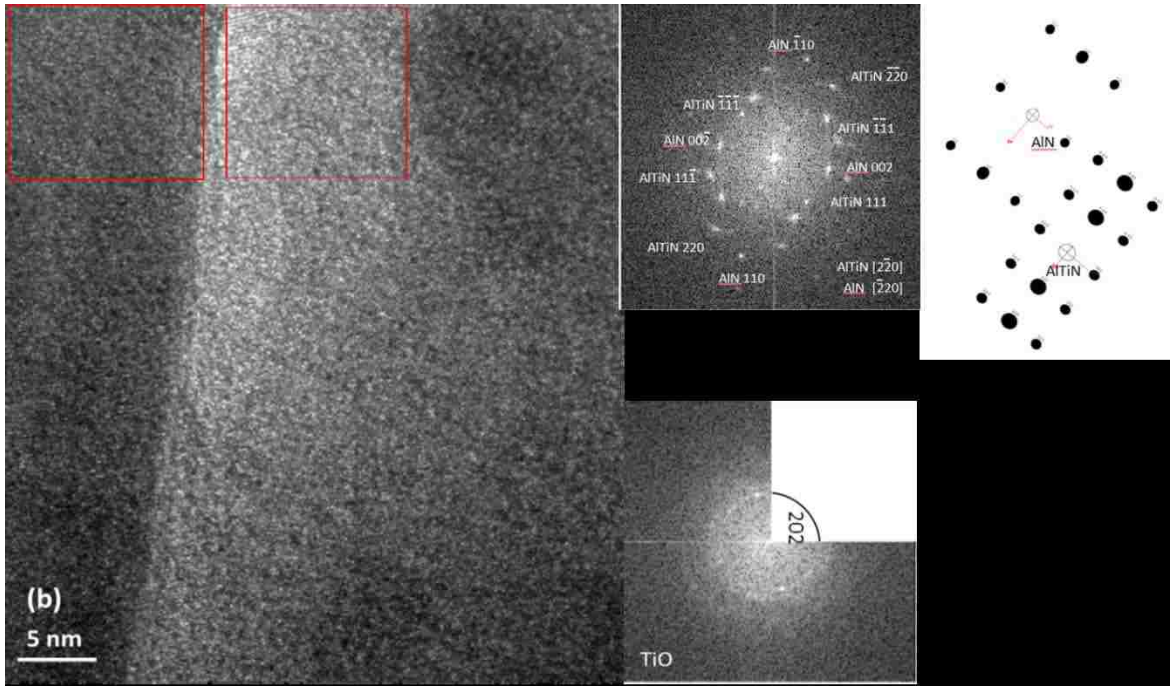
(b)
5 nm
AlN 110
AlTiN 220
AlTiN 111
AlN 002
AlTiN 111
AlN 002
AlTiN 111
AlTiN 220
AlN 110
AlTiN [2$\bar{2}$0]
AlN [$\bar{2}$20]
AlN
AlTiN
TiO
202

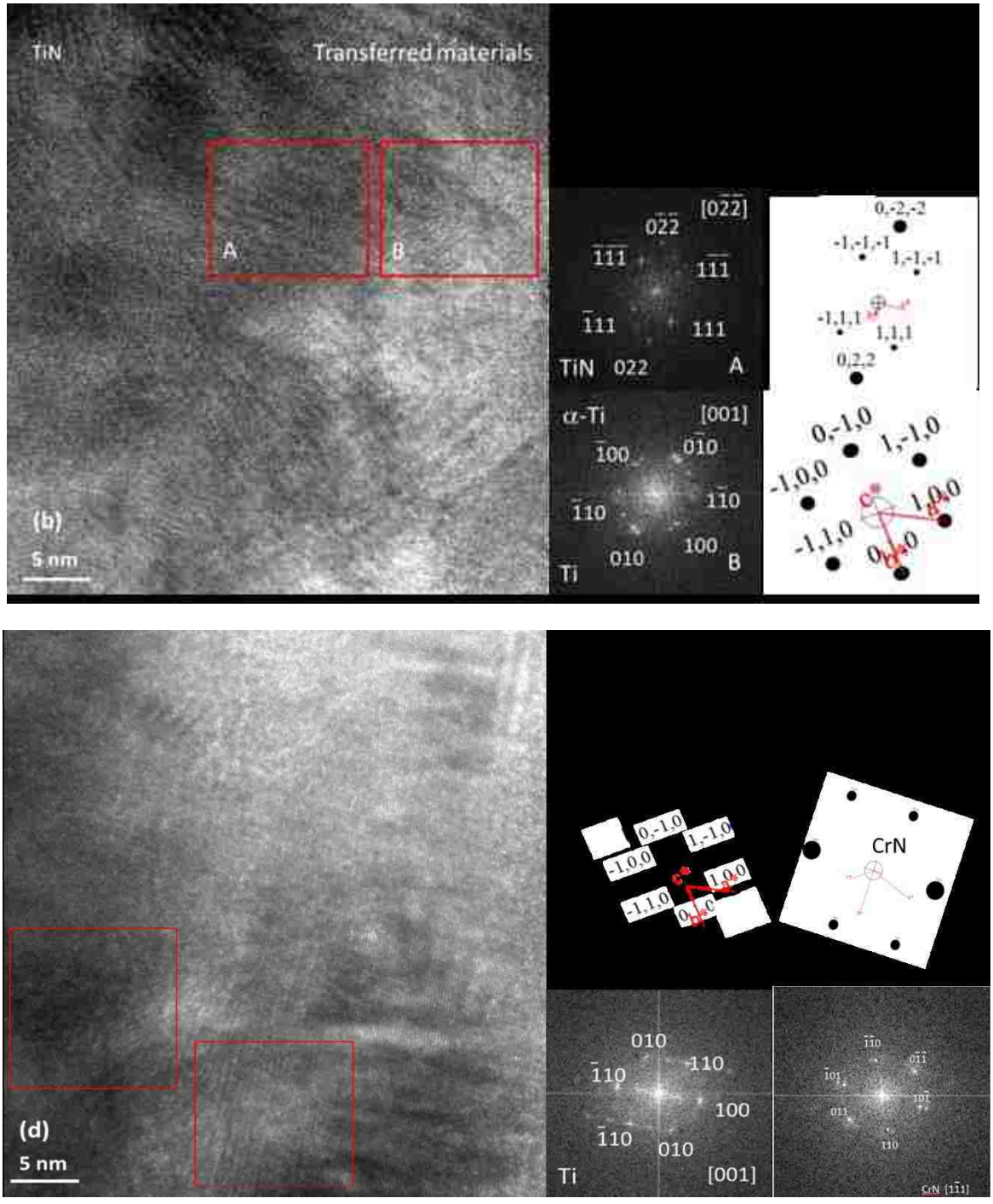

Figure 4.14 High resolution TEM (HRTEM) images and the corresponding fast Fourier transform (FFT) patterns of the transfer layer interface with (a) steel, (b) AlTiN, and (c) TiN and (d) CrN counterface balls after adhesion tests. The enclosed areas are the locations where FFT patterns were acquired showing the presence of nanocrystalline TiO at the transfer layer interface with steel and AlTiN and the presence of ultrafine α-titanium at the transfer layer/TiN, CrN interface

CHAPTER 5 DISCUSSION

5.1 Friction and adhesion behavior of Ti-6Al-4V

The weight loss of titanium after the 10-meter ball-on-disk tests (figure 4.1) demonstrate that titanium suffers high wear rate in the unlubricated condition, which can be attributed to the adhesion, abrasion and oxidation mechanisms. The results of the 10-meter ball-on-disk tests (figure 4.2 to figure 4.4) indicate the massive adhesion and transfer of Ti-6Al-4V to the counterface surfaces. Abrasion grooves on the wear tracks (figure 4.2) indicate that abrasion wear took place in the following sliding process. The plates-like and cutting-like debris in figure 4.3 also indicate that titanium alloys are severely deformed. The presence of oxygen in the fine equiaxed wear debris indicates that oxidation wear also took place during the sliding contact. The extensive material transfer to the counterface materials indicates that the adhesion wear was also the responsible wear mechanisms. The mechanisms involved in longer sliding distance were fragmentation of transfer layers, generation of debris, their oxidation between the contact surfaces which act as third body abrasive particles [56-58].

As shown in figure 4.6, Ti-6Al-4V demonstrated a severe adhesive wear in the adhesion tests. The results also show that the adhesion and transfer of Ti-6Al-4V to different counterface surfaces initiated at an early stage of sliding. The presence of transfer layers on the counterface balls (figure 4.6) without generation of loose debris after adhesion tests indicate that at the early stage of sliding, adhesion is the dominate

mechanism in controlling the friction. The mechanisms involved in longer sliding distance can be related to the fragmentation of transfer layers, generation of debris, their oxidation between the contact surfaces (figure 4.3) and their act as third body abrasive particles [14, 15], thus leads to the high wear rate of Ti-6Al-4V in sliding contact.

The initial stage of sliding, marked in the coefficient of friction (COF) vs. sliding distance plots (figure 4.10), can help to identify the responsible wear mechanisms at the beginning of sliding. Different durations of this stage for AISI 52100 steel and nitride coatings may correspond to several factors such as surface topography, frictional heating, formation of adhesive junctions, and destruction of surface layers [16]. Since the initial surfaces were of similar roughness values (Table 4.1), the friction behavior of each tested system during the initial stage of sliding represents the formation of adhesive junctions between Ti-6Al-4V and steel, AlTiN, TiN, and CrN. This is also confirmed by analytical microscopy investigations performed at the interfacial regions (figure 4.13). For steel a threshold friction force of 1.05 N was reached after a sliding distance of 2.0 mm. AlTiN coating reached their threshold force values (1.27 N) after sliding distances of 3.5 mm. However, for CrN a threshold friction force of 1.23 N was reached after a sliding distance of 0.2 mm and TiN coating reached their threshold force values (1.20 N) after distances of 0.7 mm. The short distance for TiN and CrN likely indicates that asperity junctions formed between Ti-6Al-4V and TiN, CrN are soon detached after sliding initiated. This is also confirmed by presence of lateral microcracks at the interfacial

region between the transfer layers on TiN coating (figure 4.9 d). Furthermore, a drop in the COF of Ti-6Al-4V curve appears to be due to the removal of the transfer layer. The fast removal of titanium transfer layer from the TiN and CrN surface exposed the contact region to fresh titanium surfaces, thus leading the increase of coefficient of friction.

The friction force between Ti-6Al-4V and the counterface surfaces can be attributed to adhesion and ploughing force and related to the strength of junctions between Ti-6Al-4V and the counterface surfaces [32-34]. It has been demonstrated that the friction force due to adhesion can be expressed by Equation (2) [34], where L is the normal force.

$$F_a = \frac{1}{6}L \qquad (2)$$

The ploughing factor can be calculated using the following equation [35]:

$$F_p = \frac{1}{12}\frac{d^2}{r}p \qquad (3)$$

Where d is the width of the wear track, r is the ball radius and p is the shear strength of Ti-6Al-4V. Thus, it is expected that the friction force is mainly controlled by the properties of Ti-6Al-4V, because of its lower hardness compared to the counterface and strong tendency to transfer to the counterface. Therefore, the friction force is consisted of:

$$F_f = F_a + F_p = \frac{1}{6}L + \frac{1}{12}\frac{d^2}{r}p \qquad (4)$$

Using the experimental parameters of d = 0.1 mm, $F_f \approx 1.35$ N, r = 6 mm L = 3 N, and p = 600 MPa [25] the ratio of adhesion factor and ploughing factor can be calculated

as follows:

$$k = \frac{F_a}{F_p} = \frac{\frac{1}{6}L}{\frac{1}{12}\frac{d^2}{r}p} = 0.6 \qquad (5)$$

The calculation result shows that adhesion contributed slightly more than half to the ploughing in controlling the friction force. Thus, it is suggesting that the strength of the junctions was higher than the cohesive strength of the alloy [18].

5.2 Investigation on the interface between transfer layer and counterface materials

Characterization of the transfer layers by combined TEM/diffraction patterns and electron energy loss spectroscopy (EELS) maps in figure 4.11 revealed layered structures composed of nanocrystalline oxides embedded in an amorphous Ti-6Al-4V matrix. The amorphous microstructure suggested that Ti-6Al-4V experienced localized severe plastic deformation at the contact areas. The incorporation of oxide particles in the transfer layers (figure 4.12) also indicated that tribo-oxidation was an additional dominant mechanism. The onset of transfer phenomenon during the initial stage of sliding was influenced by the counterface material. The initial stage of sliding shown in the coefficient of friction vs. sliding distance plots (figure 4.10) correspond to the formation of adhesive junctions between Ti-6Al-4V and steel and TiN coatings during which frictional force gradually increases to a peak value corresponding to the “threshold force” where the junctions break and COF declines [59] and the friction force between Ti-6Al-4V and the counterface surfaces can be attributed to adhesion and ploughing force

and related to the strength of junctions between Ti-6Al-4V and the counterface surfaces [3].

The scanning transmission electron microscopy (STEM) images and corresponded convergent beam electron diffraction (CBED) patterns of the transferred material to AISI52100 steel were shown in figure 4.11 a. The results indicated that the microstructure of the transfer layer on AISI 52100 steel consists a lamellar structure. It has layered amorphous matrix with layered nanocrystalline and polycrystalline structures embedded in. The top layer in the transferred material to (inserts 1-3 in figure 4.11 a) indicated a amorphous oxides layer existing at the top of transferred layer. Polycrystalline oxides (inserts 4 and 6 in figure 4.11 a) and nanocrystalline oxides (inserts 5 and 7 in figure 4.11 a) were observed underneath the top layer. The scanning transmission electron microscopy (STEM) images and corresponded convergent beam electron diffraction (CBED) patterns of the transferred material to AlTiN coating were shown in figure 4.11 b. The convergent beam electron diffraction patterns indicate that the oxides in the transferred material have both nanocrystalline (inserts 1, 2, 3, 5 and 7 in figure 4.11 b) and polycrystalline microstructure (4 and 6 figure 4.11 b). The polycrystalline structures embedded in the amorphous matrix. The scanning transmission electron microscopy (STEM) images and corresponded convergent beam electron diffraction (CBED) patterns of the transferred material to TiN coating were shown in figure 4.11 c. It has layered amorphous matrix (inserts 1, 2, 3, 5 and 7 in figure 4.11 c) with thin

nanocrystalline and polycrystalline structures (inserts 4 and 6 in figure 4.11 c) embedded in. The scanning transmission electron microscopy (STEM) images and corresponded convergent beam electron diffraction (CBED) patterns of the transferred material to CrN coating were shown in figure 4.11 d. The convergent beam electron diffraction patterns indicate that the top layer amorphous microstructure (inserts 1 to 5 figure 4.11 d) while the embedded oxides underneath the top layer showed a nanocrystalline and polycrystalline microstructure.

The electron energy loss spectroscopy (EELS) maps constructed from the cross section of transfer layers (figure 4.12) confirmed that the transferred material was consisted of layers composed contained of Ti, V, Al, and O (nanocrystalline oxides). It was observed that the transferred materials to the TiN and CrN coating counterface (figure 4.12 c and d) contain finer oxides layers compared to the steel and AlTiN counterface (figure 4.12 a and b). This result indicated that the transferred material to TiN and CrN counterface was less severely oxidized when compared to the transferred material to steel and AlTiN counterface.

The presence of TiO at the interface of steel and AlTiN counterface balls with the transfer layer (figure 4.13 a and b) as well as longer durations at the initial stage of sliding observed in the COF curves (figure 4.10) implied formation of stronger junction bonds and higher affinity of titanium for adhesion to steel and AlTiN surfaces. As such the asperities had sufficient time to oxidize under sliding contact.

A closer examine of the nanocrystalline oxides in the transferred material using the electron diffraction patterns taken from several different locations within the higher oxygen content area in transfer layers (figure 4.14) indicated that regions with a higher oxygen content, contained titanium oxide (TiO, space group C2/m) and vanadium oxide (V_2O_3, C2/c space group) for existed in the transfer layer on steel surface. However, only nanocrystalline titanium oxide (TiO, space group C2/m) observed in the transfer layer on the coating surfaces. The absence of vanadium oxides in the transfer layer on coating surfaces can be related to the less severe oxidized nature of the transferred material on coating surface as show in figure 4.14.

The fast removal of titanium transfer layer from the CrN surface exposed the contact region to fresh titanium surfaces. This was accompanied by detection of an ultrafine α-titanium structure at the CrN/transfer layer interface using high resolution TEM (HRTEM) images and fast Fourier transform (FFT) patterns (figure 4.13 c). Similar microstructures have been reported for adiabatic shear bands in titanium alloys [29-31]. This was accompanied by detection of an ultrafine α-titanium structure at the CrN/transfer layer interface using high resolution TEM (HRTEM) images and fast Fourier transform (FFT) patterns (figure 4.13 c). Similar microstructures have been reported for adiabatic shear bands in titanium alloys [60-62].

For steel surface, the large misfit between steel and α-titanium leads to severe plastic deformation, which will promote oxidation by input deformation energy. In

addition, the small misfit between iron lattice and TiO lattice can also promote the oxidation of transfer layer. The preferred orientation between iron and TiO is the {202} planes of TiO to the {011} planes of iron. The misfit between this two plane groups can be calculated as

$$\frac{0.2098 - 0.2027}{0.2098} \times 100\% = 3.38\%$$

The oxides formed at the interface will in turn slightly reduce the COF in this stage of sliding tests.

AlTiN coating has mix microstructure of polycrystalline AlN and AlTiN. The large misfit between {220} planes of AlTiN, {110} planes of AlN planes and α-titanium planes leads to severe plastic deformation. The high hardness of AlTiN coating also results in severe plastic deformation ofα-titanium.

The observations ofα-titanium can be attributed to a less lattice misfit of TiN and α-titanium crystal compared to steel and α-titanium crystal, which means that the planes on TiN coating, where the α-titanium was observed possessed similar d-spacing value to α-titanium [60]. That is also the reason why the COF is higher when TiN sliding against Ti-6Al-4V. Because two solid surface with small misfit sliding against each other often results in strong adhesion and high COF [61, 62]. The preferred orientation relationship of transferred Ti to TiN is the {110} planes of titanium to {111} planes of TiN. The misfit between these two plane groups can be calculated as

$$\frac{0.2494 - 0.2313}{0.2494} \times 100\% = 7.25\%$$

The preferred orientation relationship of transferred Ti to CrN is the {110} and {010} planes of titanium to {110} planes of CrN. The misfit between these two plane groups can be calculated as

$$\frac{0.2413 - 0.2313}{0.2413} \times 100\% = 4.14\%$$

The calculations of lattice misfit indicates that the d-spacing of TiN and CrN crystals are close to that of α-titanium, which can explain the presence of α-titanium at the interface of the transfer layer and counterface materials. The d-spacing of AISI 52100 steel and AlTiN is close to that of TiO, which can explain the presence TiO at the interface. The shorter sliding distance for coefficient of friction to reach the threshold value when sliding against TiN and CrN coatings can be correlated to the presence of α-titanium at the interface. The less adhesion of Ti-6Al-4V to these coatings is observed as well. An lateral crack is observed at the interface between the transfer layer and CrN coating, which suggests α-titanium is easier to remove compared to TiO during the following sliding process because of the combination of work hardening and severe plastic deformation [63].

In summary, TiN and CrN coatings show better performance in reducing the oxidation and adhesion of Ti-6Al-4V under unlubricated sliding condition.

CHAPTER 6 CONCLUSIONS AND RECOMMENDATIONS

6.1 Conclusions

The adhesion behavior of Ti-6Al-4V against AISI 52100 steel, AlTiN, TiN and CrN counterfaces under unlubricated sliding condition was studied and compared to investigate the micro adhesion mechanisms at the initial state of sliding contact. Conclusions are presented below:

- Ti-6Al-4V transferred extensively to uncoated AISI 52100 steel and PVD ceramic coatings, however, the wear rate of Ti-6Al-4V is lower when sliding against TiN and CrN coatings, which can be related to a less severe material transfer during the initial stage of sliding.
- Severe adhesion of Ti-6Al-4V to AISI 52100 steel, AlTiN, TiN and CrN occurred during the initial stage in sliding contact, however, the coefficient of friction curve shows that when sliding against CrN and TiN coatings the coefficient of friction reached the threshold value within shorter distance compared to when sliding against AISI 52100 steel and AlTiN counterface.
- Analytical microscopy investigations revealed that the transferred material has a lamellar amorphous structure. Both TiO and V_2O_3 is observed in the high oxygen content regions on the transfer layer to steel, however, only TiO is observed in transfer layer to PVD coatings. This observation suggests that Ti-6Al-4V is less severely oxidized when sliding against PVD coatings. The

less severe oxidation of Ti-6Al-4V can be used to explain the shorter distance of the coefficient of friction to reach the threshold value when sliding against TiN and CrN coating.

- Ti-6Al-4V showed lowest transferred volume to CrN coating. This result can be related to the small lattice misfit between the CrN and α-titanium crystal. This observation suggests the d-space of the counterface material should be selected close to the d-space of α-titanium to reduce the oxidation and adhesion of Ti-6Al-4V.

6.2 Recommendations for future research

The following works are suggested for future research:

- α-titanium and TiO are observed at the interface region, however, no β titanium particles are observed. Thus, it is interesting to perform the adhesion tests on the β titanium alloy and compare its adhesion behavior and mechanisms to the α + β titanium alloy.
- Computer simulation of the adhesion of titanium alloy to different counterface materials is a promising method to verify the experimental observation and provide quantified results to predict the adhesion of Ti-6Al-4V.
- Lubricants can reduce the adhesion of titanium alloys. It is also interesting to research effects of different lubricate conditions on the adhesion mechanisms of Ti-6Al-4V during the initial stage of material transfer.

Appendix A: Copyright Permission

ELSEVIER LICENSE

Jan 26, 2015

Supplier: Elsevier Limited

The Boulevard, Langford Lane

Kidlington, Oxford, OX5 1GB,UK

License number 3556540049844

License date: Jan 26, 2015

Licensed content publisher: Elsevier

Licensed content publication: Surface and Coatings Technology

Licensed content title: Investigation on interfacial adhesion of Ti–6Al–4V/nitride coatings

Licensed content date: 15 December 2014

Licensed content volume number: 260

Number of pages: 13

Start Page: 155

End Page: 167

Type of Use reuse: in a thesis/dissertation

Portion: full article

Format: both print and electronic

Are you the author of this Elsevier article? Yes

Will you be translating? No

TERMS AND CONDITIONS

Elsevier supports the need for authors to share, disseminate and maximize the impact of their research and these rights, in Elsevier proprietary journals are defined below:

Authors transfer copyright to the publisher as part of a journal publishing agreement, but have the right to:

i. Share their article for personal (scholarly) purposes (including scholarly rights to create certain derivative works), so long as they give proper attribution and credit to the published work:

Authors can use their articles, in full or in part, for a wide range of scholarly, non-commercial purposes as outlined below:

- Share copies of the article and distribute them via email to colleagues for their research use (also known as 'scholarly sharing').
- Share the article for personal use or for the author's own classroom teaching.
- Use the article at a conference, meeting or for teaching purposes.
- Allow the author's employers to use the article for other internal purposes (such as training).
- Include the article in a printed compilation of the author's works, such as

collected writings and lecture notes.

- Inclusion the article in a thesis or dissertation
- Use the article in full or in part to prepare other derivative works, including expanding the article to book-length form, with each work to include full acknowledgement of the article' original publication.

ii. Retain patent, trademark and other intellectual property rights (including raw research data).

iii. Proper attribution and credit for the published work.

Elsevier B.V

REFERENCES

[1] G. Lütjering, J.C. Williams, Titanium, Springer, New York, 2003.
[2] C. Leyens, M. Peters, Titanium and titanium alloys, Wiley Online Library, 2003.
[3] R. Boyer, E. Collings, Materials properties handbook: titanium alloys, ASM international, 1993.
[4] M.J. Donachie, Titanium: a technical guide, ASM international, 2000.
[5] K.G. Budinski, Wear 151 (1991) 203-217.
[6] P. Miller, J. Holladay, Wear 2 (1958) 133-140.
[7] A. Molinari, G. Straffelini, B. Tesi, T. Bacci, Wear 208 (1997) 105-112.
[8] G. Straffelini, A. Molinari, Wear 236 (1999) 328-338.
[9] Y. Liu, D. Yang, S. He, W. Wu, Materials characterization 50 (2003) 275-279.
[10] H. Dong, T. Bell, Wear 225-229, Part 2 (1999) 874-884.
[11] J. Qu, P.J. Blau, T.R. Watkins, O.B. Cavin, N.S. Kulkarni, Wear 258 (2005) 1348-1356.
[12] S.H.I. Jaffery, P.T. Mativenga, The International Journal of Advanced Manufacturing Technology 58 (2012) 479-493.
[13] A. Jawaid, S. Sharif, S. Koksal, Journal of Materials Processing Technology 99 (2000) 266-274.
[14] S. Krol, L. Ptacek, Z. Zalisz, M. Hepner, Journal of Materials Processing Technology 157-58 (2004) 364-369.
[15] M.O. Alam, A.S.M.A. Haseeb, Tribology International 35 (2002) 357-362.
[16] P.J. Blau, Tribology International 38 (2006) 1007-1012.
[17] J. Ferrante, J.R. Smith, J.H. Rose, Tribology Series 7 (1981) 19-30.
[18] F.P. Bowden, D. Tabor, The friction and lubrication of solids, Clarendon Press 1986, p. 88-100.
[19] B. Derjaguin, V. Muller, Y.P. Toporov, Journal of Colloid and interface science 53 (1975) 314-326.
[20] J. Archard, Journal of applied physics 24 (1953) 981-988.
[21] E. Rabinowicz, D. Tabor, Proceedings of the Royal Society of London. Series A. Mathematical and Physical Sciences 208 (1951) 455-475.
[22] J. Zhong, R. Shakiba, J.B. Adams, Journal of Physics D: Applied Physics 46 (2013) 055307.
[23] P.J. Blau, Journal of tribology 109 (1987) 537-543.
[24] F.P. Bowden, D. Tabor, (1950).
[25] C.M. Mate, Tribology on the small scale : a bottom up approach to friction, lubrication, and wear Oxford University Press, 2008, p. 130-137.
[26] V.L. Popov, Contact mechanics and friction, Springer, 2010.
[27] K. Holmberg, A. Matthews, H. Ronkainen, Tribology International 31 (1998) 107-120.

[28] J. Klomp, P. Vrugt, Interfaces between metals and ceramics, Surfaces and Interfaces in Ceramic and Ceramic—Metal Systems, Springer, 1981, pp. 97-105.
[29] D.H. Buckley, K. Miyoshi, Wear 100 (1984) 333-353.
[30] K. Miyoshi, Adhesion, friction, and wear behavior of clean metal-ceramic couples, National Aeronautics and Space Administration, Cleveland, OH (United States). Lewis Research Center, 1995.
[31] L.-H. Lee, Fundamentals of adhesion, Springer, 1991.
[32] G.E. Vergason, Electric arc vapor deposition device, Google Patents, 1991.
[33] S. Rossnagel, J. Hopwood, Journal of Vacuum Science & Technology B 12 (1994) 449-453.
[34] Y. Chim, X. Ding, X. Zeng, S. Zhang, Thin Solid Films 517 (2009) 4845-4849.
[35] H. Tönshoff, A. Mohlfeld, Surface and Coatings Technology 93 (1997) 88-92.
[36] P. Jindal, A. Santhanam, U. Schleinkofer, A. Shuster, International Journal of Refractory Metals and Hard Materials 17 (1999) 163-170.
[37] E. Ezugwu, C. Okeke, Journal of Materials Processing Technology 116 (2001) 10-15.
[38] Y. Guu, H. Hocheng, Materials Science and Engineering: A 318 (2001) 155-162.
[39] T.-R. Lin, Journal of Materials Processing Technology 127 (2002) 8-16.
[40] T. Ueda, M. Al Huda, K. Yamada, K. Nakayama, H. Kudo, CIRP Annals-Manufacturing Technology 48 (1999) 63-66.
[41] S. PalDey, S. Deevi, Materials Science and Engineering: A 342 (2003) 58-79.
[42] H. Prengel, W. Pfouts, A. Santhanam, Surface and Coatings Technology 102 (1998) 183-190.
[43] B. Warcholinski, A. Gilewicz, J. Ratajski, Tribology International 44 (2011) 1076-1082.
[44] S. Pradhan, C. Nouveau, A. Vasin, M.-A. Djouadi, Surface and Coatings Technology 200 (2005) 141-145.
[45] S. Shin, M. Kim, M. Kang, K. Kim, D. Kwon, J. Kim, Surface and Coatings Technology 202 (2008) 5613-5616.
[46] F. Klocke, N. Michailidis, K.-D. Bouzakis, M. Witty, S. Gerardis, E. Lili, M. Pappa, Production Engineering 4 (2010) 509-514.
[47] Z. Wang, E. Ezugwu, Tribology transactions 40 (1997) 81-86.
[48] C. Che-Haron, A. Jawaid, Journal of Materials Processing Technology 166 (2005) 188-192.
[49] A. Hosokawa, K. Shimamura, T. Ueda, CIRP Annals-Manufacturing Technology 61 (2012) 95-98.
[50] D.M. Mattox, Handbook of physical vapor deposition (PVD) processing, William Andrew, 2010.
[51] A. Jawaid, S. Sharif, S. Koksal, Journal of Materials Processing Technology 99 (2000) 266-274.

[52] E. Ezugwu, I. Pashby, Journal of materials processing technology 33 (1992) 429-437.
[53] S. Carvalho, E. Ribeiro, L. Rebouta, C. Tavares, J. Mendonça, A. Caetano Monteiro, N. Carvalho, J.T.M. De Hosson, A. Cavaleiro, Surface and Coatings Technology 177 (2004) 459-468.
[54] L. Dobrzański, K. Gołombek, Journal of Materials Processing Technology 164 (2005) 805-815.
[55] P.J. Blau, Wear 71 (1981) 29-43.
[56] M. Long, H. Rack, Wear 249 (2001) 157-167.
[57] F. Stott, Tribology International 31 (1998) 61-71.
[58] C. Hager Jr, J. Sanders, S. Sharma, Wear 257 (2004) 167-180.
[59] A.R. Riahi, A. Edrisy, A.T. Alpas, Surface & Coatings Technology (2009) 2030–2035.
[60] S. Timothy, I. Hutchings, Materials science and technology 1 (1985) 526-530.
[61] J. Hershberger, O. Ajayi, J. Zhang, H. Yoon, G. Fenske, Wear 258 (2005) 1471-1478.
[62] N. Chelliah, S.V. Kailas, Wear 266 (2009) 704-712.
[63] W.-S. Lee, C.-F. Lin, Materials Science and Engineering: A 241 (1998) 48-59.

VITA AUCTORIS

NAME: Liang Jin

PLACE OF BIRTH: Harbin, China

DATE OF BIRTH: 1989

EDUCATION: Bachelor of Engineering,

Material Science and Engineering

Southwest Jiaotong University

Chengdu, Sichuan, China

2012

Master of Applied Science

Engineering Materials

University of Windsor

Windsor, ON, Canada

2015